

# Turbulence in the Inter-galactic Medium: Solenoidal and Dilatational Motions, and the Impact of Numerical Viscosity

Weishan Zhu<sup>1,2</sup>, Long-long Feng<sup>3</sup>, Yinhua Xia<sup>4</sup>, Chi-Wang Shu<sup>5</sup>, Qiusheng Gu<sup>1,2</sup> and Li-Zhi Fang<sup>6</sup>

## ABSTRACT

We use a suite of cosmological hydrodynamic simulations, run by two fixed grid codes, to investigate the properties of solenoidal and dilatational motions of the intergalactic medium (IGM), and the impact of numerical viscosity on turbulence in a LCDM universe. The codes differ only in the spatial difference discretization. We find that (1) The vortical motion grows rapidly since  $z = 2$ , and reaches  $\sim 10\text{km/s} - 90\text{km/s}$  at  $z = 0$ . Meanwhile, the small-scale compressive ratio  $r_{CS}$  drops from 0.84 to 0.47, indicating comparable vortical and compressive motions at present. (2) Power spectra of the solenoidal velocity possess two regimes,  $\propto k^{-0.89}$  and  $\propto k^{-2.02}$ , while the total and dilatational velocity follow the scaling  $k^{-1.88}$  and  $k^{-2.20}$  respectively in the turbulent range. The IGM turbulence may contain two distinct phases, the supersonic and post-supersonic phases. (3) The non-thermal pressure support, measured by the vortical kinetic energy, is comparable with the thermal pressure for  $\rho_b \simeq 10 - 100$ , or  $T < 10^{5.5}K$  at  $z = 0.0$ . The deviation of the baryon fraction from the cosmic mean shows a preliminary positive correlation with the turbulence pressure support. (4) A relatively higher numerical viscosity would dissipate both the compressive and vortical motions of the IGM into thermal energy more effectively, resulting in less developed vorticity, remarkably shortened inertial range, and leading to non-negligible uncertainty in the thermal history of gas accretion. Shocks in regions

---

<sup>1</sup>School of Astronomy and Space Science, Nanjing University, Nanjing, 210092, China

<sup>2</sup>Key Laboratory of Modern Astronomy and Astrophysics of the Ministry of Education, Nanjing, 210092, China

<sup>3</sup>Purple Mountain Observatory, Nanjing, 210008, China

<sup>4</sup>School of Mathematical Sciences, University of Science and Technology of China, Hefei, Anhui 230026, China

<sup>5</sup>Division of Applied Mathematics, Brown University, Providence, RI 02912, USA

<sup>6</sup>Department of Physics, University of Arizona, Tucson, AZ 85721, USA

outside of clusters are significantly suppressed by numerical viscosity since  $z = 2$ , which may directly cause the different levels of turbulence between two codes.

*Subject headings:* cosmology: theory - intergalactic medium - large-scale structure of the universe - methods: numerical

## 1. Introduction

The intergalactic medium (IGM) feeds the growth of galaxies and receives feedback from star formation and even more violent activity like AGN in galaxies. The dynamical and thermal states of the intergalactic medium reflect this mutual process and are important factors to interpret many observations, such as the Ly $\alpha$  forest and the metal absorption lines in the spectra of high redshift objects, which could in turn support the structure formation theory. Moreover, more information on the state of the IGM would shed light on the so-called missing baryon problem at low redshift. The observed baryons in galaxies only account for one-tenth of the cosmic baryon content that given by the high redshift Ly $\alpha$  lines and the cosmic microwave background (CMB) studies (Fukugita, Hogan, & Peebles et al. 1998; Bregman 2007 and references therein).

The thermal state of the IGM has been thoroughly studied by cosmological hydrodynamical simulations since the late 1990s. Most of those works predicted that the majority of baryons rest in the warm ( $10^4 < T < 10^5$ ), and the warm-hot ( $10^5 < T < 10^7$ ) IGM, i.e., WHIM (e.g., Cen & Ostriker 1999; Dave et al. 1999; Dave et al. 2001; Cen & Ostriker 2006). Many efforts have been made by observers to detect the WHIM in the low density regions (Bregman 2007). The dynamical state of the IGM, however, has not gained much attention. Adhesion models have been applied to describe the evolution of the distribution of baryonic gas in the mildly non-linear regimes in analytic works (Jones 1999; Matarrese & Mohayaee 2002), which, however, may only work for baryon density contrast  $< 5 \sim 10$  and can not capture the complex pattern of baryonic flow in the highly non-linear regimes. As an emerging subject, the turbulence in the IGM has invoked growing interest in recent years. Observationally, Zheng et al. (2004) fitted the H I and He II absorption lines in the high quality spectra of quasar HE 2347-4342 and found comparable velocities of hydrogen and He ions, suggesting a turbulence dominated velocity field in the IGM between  $z = 2.0$  and 2.9. Estimation of the turbulent velocity in galaxy groups and clusters are available in recent years via direct and indirect observational means, giving weakly constrained upper limits of hundreds  $\text{km s}^{-1}$  (Churazov et al. 2004; Sanders et al. 2010, 2011, 2013; Bulbul et al. 2012).

He et al. (2006) studied the intermittency of the velocity field of cosmic baryons in cosmological simulation, indicating that the motion of baryons might be turbulent on large scales. Ryu et al. (2008) found that vorticity could induce turbulent-flow motions in the IGM and amplify the intergalactic magnetic fields. Oppenheimer & Dave (2009) used cosmological simulations to model the O VI absorbers at  $z < 0.5$  and required a density-dependent sub-resolution turbulent motion in the IGM to match the observation results. Tepper-Garcia et al. (2011) also found the necessity of turbulence in the IGM that was not captured in their simulation to mimic the OVI absorbers at low redshift. In a previous paper Zhu, Feng, & Fang (2010) (hereafter ZFF2010), we studied the evolution of vorticity and its power spectrum in the IGM, and showed that the IGM is highly turbulent in the range from a couple of Mpc down to hundreds of kpc at low redshifts.

An elementary understanding about the turbulence injection in the IGM has been established, although many details remain unknown. Cosmological hydrodynamic simulations show that supersonic gas motions will develop during the hierarchical structure formation (Ryu et al. 2003; Pfrommer et al. 2006; Skillman et al. 2008; Vazza et al. 2009). Those supersonic flow motions, driven by the baryon gas accreting to sheets and filaments, and gaseous haloes merging with each other, could efficiently induce vorticity in the intergalactic velocity field and then trigger turbulence (Ryu et al. 2008; ZFF2010). In addition to the cosmological shocks and vorticity, the shear flows produced by the ram pressure stripping of protogalactic and collapsed objects moving in the IGM will bring turbulent motions too. Also, galactic outflows driven by starburst and AGN might inject turbulent kinetic energy into cluster outskirts (Evoli & Ferrara 2011). Iapichinio et al. (2011) used sub-grid scale model to include the unresolved small scale turbulence in their analysis of turbulent kinetic energy evolution as a function of redshifts, and speculated that shock interactions and merger induced shear flows should be the main source for the production of turbulence in the WHIM and ICM, respectively.

Meanwhile, properties of compressible and supersonic isotropic turbulence in the context of fluid dynamics and interstellar medium study have been investigated in more details in the past two decades (e.g., Kida & Orszag 1990, 1992; Porter et al. 1992, 1994, 1998; Kritsuk et al. 2007; Federrath et al. 2010). Statistics of velocity and its two components, including power spectra and structure functions, show that both decaying and forced supersonic turbulence behave differently from incompressible Kolmogorov-type turbulence. As the turbulence in the IGM is likely mainly produced by cosmic shocks, its scaling law may also deviate from the classical Kolmogorov’s. Actually, the power spectra of the velocity (Ryu et al. 2008, He et al. 2006) and kinetic energy (ZFF2010) of the IGM have already exhibited non-Kolmogorov features.

Moreover, the velocity field of the IGM would be dilatationally dominated at high redshifts, because the driving force, gravity, is curl-free. As vortices emerge at low redshifts, the velocity field would transfer into solenoidal domination within the turbulence inertial range, driven by dilatational forcing. The evolution of vorticity and divergence, and their corresponding velocity components, solenoidal and dilatational velocity, would be an essential probe to the transfer process. More solid results concerning those fundamental characteristics can enrich and verify our knowledge of turbulence in the IGM.

On the other hand, the numerical viscosity in cosmological hydrodynamic simulation codes may have a significant impact on the development of turbulence in the IGM. Because of the relatively low density in comparison with the Earth’s gas, the IGM is estimated to have very high Reynolds number( e.g.  $10^{13}$  in Gregori et al. 2012). For the hot intra-cluster medium, however, the physical viscosity may be non-negligible. Fabian et al. (2003a,b) gave an estimated Reynolds number of  $\sim 1000$  in the central region of the Persues cluster, and suggested that the viscosity dissipation would be important in the inner tens of kpc. The physical viscosity of the ICM have been considered and implemented into cluster formation simulations(e.g., Sijacki& Springel 2006; Dong&Stone et al. 2009; Suzuki et al. 2013). Otherwise, the cosmic gas component is usually assumed to be non-viscous and governed by the cosmological version of the Euler equation. Despite that many efforts have been made to reduce it, numerical viscosity remains non-negligible in almost all of the codes and bring additional numerical dissipation with respect to the physical dissipating mechanisms including Jeans dissipation and shock heating. Numerical viscosity will damp the flow instabilities and shock waves, and smearing out substructure in cosmological hydrodynamic simulations, which has been confirmed by many code comparison works (e.g., Agertz et al. 2007; Vazza et al. 2011; Bauer & Springel, 2012). Dolag et al. 2005 found that the numerical viscosity in the smoothed particle hydrodynamics (SPH) method can artificially suppress the turbulent motions in the intra-cluster medium. Nelson et al. (2013) proposed that the turbulent motions on large scales could be spuriously dissipated into thermal energy by numerical viscosity, which would keep the baryonic gas locked in the diffuse, hot and low density halos of central galaxies, and consequently slow down the hot gas accretion by an order of magnitude. Hence, the various levels of numerical viscosity in different codes are expected to lead to different intensity of turbulence in the IGM. To obtain a more concrete understanding of turbulence in the IGM, the impact of numerical viscosity needs to be investigated comprehensively.

Using two kinds of fixed mesh methods with different levels of numerical viscosity, we performed a suite of high resolution cosmological hydrodynamical simulations to investigate the properties of solenoidal and dilatational velocity fields, and made comparison between two codes regarding turbulence and shocks development in the IGM. Differences between samples run by these two codes allowed us to assess the impact of numerical viscosity, and

in turn provided more details on the production and evolution of turbulence, which would help to build a more reliable history of gas accreting onto virialized structures.

This paper is organized as following. In §2, we give a short introduction to the numerical methods used in this work and then present some simulation details. §3 investigates the properties of vorticity and divergence in the IGM in our simulation samples. Statistics of solenoidal and dilatational velocity, and non-thermal pressure provided by the solenoidal motion are studied in §4. Then we analyze the distribution of cosmic shocks in simulations run by these two different schemes with the same resolution in §5. Discussion and concluding remarks are summarized in §6. The numerical tests for code comparison and resolution convergence are presented in the Appendix.

## 2. Numerical Methods

### 2.1. TVD scheme

In the literature, many modern difference schemes are referred as total variation diminishing (TVD) method, as long as they fulfill the TVD nonlinear stability condition for scalar model problems and linear systems, which was first suggested by Harten (1983). In this work, we will use Harten’s original, explicit, second-order TVD scheme, and expand it to three dimension by dimension splitting(Strang 1968). This scheme will be implemented into the cosmological context in almost the same way as in Ryu et al. (1993), except for the treatment of internal energy in order to improve its performance in high Mach number regions. Usually, non-negligible errors may appear in hypersonic regions if the thermal energy is calculated by subtracting the kinetic energy from the total energy, and sometimes this leads to negative density and pressure. In Ryu et al. (1993), a modified entropy method was used to solve the thermal energy accurately. In this work, we employ the entropy based dual energy method in Feng et al. (2004) to track the thermal energy for the TVD scheme.

### 2.2. Positive-Preserving WENO Scheme

The weighted essentially non-oscillatory (WENO) scheme is a high-order finite difference scheme first developed by Jiang & Shu (1996). The WENO scheme can simultaneously achieve high order accuracy in smooth region, and sharp transition at shock or contact discontinuity surface (Shu 1998, 1999). Feng et al. (2004) implemented the fifth order finite difference WENO scheme into the context of cosmological application and demonstrated its capacity of capturing strong shocks and complex flow pattern emerging in cosmic structure

formation.

Very recently, Zhang & Shu (2012) designed a positivity-preserving strategy combining with high order finite difference WENO scheme, which could successfully keep the positivity of density and pressure during simulation without losing conservation and high order accuracy, and highly improved the performance of the WENO scheme in solving hypersonic flows. Details about the positive-preserving WENO scheme can be found in the Appendix. The global Lax-Friedrichs flux splitting method is used in this work, which is more robust and compatible with the positivity-preserving method than the local Lax-Friedrichs flux splitting used in ZFF2010. This change results in a looser restriction on the  $cfl$  number and less dispersion over spherical shock front, shown by the Sod shock tube, and Sedov blast wave tests presented in the Appendix, where the performance of the WENO and TVD schemes are given.

### 2.3. Cosmological Simulation Set Up

We use the WENO and TVD schemes for ideal fluid dynamics, coupled with the standard particle-mesh method for gravity calculation. In particular, the early WENO scheme employed in Feng et al.(2004) is updated with the positivity-preserving version, which maintains the positivity of physical quantities. Except for the spatial difference discretizations, all the other modules are the same in both codes, including the gravity solver, time difference scheme, cooling and heating processes. The time integrations are performed using the third order low storage Runge-Kutta method.

All the cosmological simulations are performed in a periodic cubic box of size  $25 h^{-1}$  Mpc in a LCDM universe. The cosmological parameters are set to the WMAP5 result (Komatsu et al. 2009), i.e.,  $(\Omega_m, \Omega_\Lambda, h, \sigma_8, \Omega_b, n_s) = (0.274, 0.726, 0.705, 0.812, 0.0456, 0.96)$ . We run simulations with equal number of grid cells and dark matter particles, one set with  $512^3$  evolved by the WENO and TVD schemes respectively, and another with  $1024^3$  evolved by the WENO scheme only. The  $512^3$  runs have a grid resolution of  $47.7 h^{-1}$  kpc, and a mass resolution of  $1.04 \times 10^7 M_\odot$  for the dark matter particle. The effect of re-ionization is included by adding a uniform UV background that is switched on at  $z = 11.0$ , and the radiative cooling and heating processes are modeled in the same way as Theuns et al. (1998), with a primordial composition ( $X = 0.76, y = 0.24$ ). Star formation and its feedback are not taken into account. All the simulations start at redshift 99 and end at 0, We will refer a specific simulation run in the form of, e.g., 'WENO-512', where the terms before and after the dash stand for the hydro scheme and one-dimensional scale, respectively.

### 3. Vorticity and Compressibility in the IGM

In Ryu et al. (2008) and ZFF2010, the vorticity of the IGM velocity field and its power spectra have been demonstrated to be good indicators of turbulence. This section is to investigate the behavior of these indicators in our simulation samples. As a useful probe to the growth history of solenoidal motions with respect to dilatational motions under a curl-free forcing, the relative importance of vorticity to divergence will also be addressed by the small scale compressive ratio.

#### 3.1. Vorticity Distribution

The vorticity of the IGM velocity field is defined as  $\vec{\omega} = \nabla \times \mathbf{v}$ . The dynamical equation of the modules of vorticity vector,  $\omega \equiv |\vec{\omega}|$ , in the IGM reads as (ZFF2010)

$$\frac{D\omega}{Dt} \equiv \partial_t \omega + \frac{1}{a} \mathbf{v} \cdot \nabla \omega = \frac{1}{a} \left[ \alpha \omega - d\omega + \frac{1}{\rho^2} \vec{\xi} \cdot (\nabla \rho \times \nabla p) - \dot{a} \omega \right], \quad (1)$$

where  $\vec{\xi} = \vec{\omega}/\omega$ ,  $\alpha = \vec{\xi} \cdot (\vec{\xi} \cdot \nabla) \mathbf{v}$ , and  $d = \partial_i v_i$  is the divergence of the velocity field.

According to eqn.(1), the generation of vorticity in the IGM can be attributed to the baroclinity term,  $(1/\rho^2) \nabla \rho \times \nabla p$ . A non-zero baroclinity means the gradient of pressure and density are not parallel to each other, which occurs in curved shocks and complex flow structures. Stretched by the first term on the right hand side (RHS) of Eq(1), the vorticity structures will expand or contract along the local baryon gas flow. Meanwhile, the vorticity in the IGM will be attenuated by the cosmic expansion. Normalized by the cosmic time  $t$ , the vortical motion of fluid is usually measured by the dimensionless quantity  $\omega t$ , which actually characterizes the number of turn-overs that vortices can make within the cosmic time.

Figure 1 presents a straightforward view of the distribution of dark and baryonic matter, and vorticity in a slice of depth  $250h^{-1}$  kpc, which are extracted from the WENO-512 and TVD-512 simulation samples respectively. The dark matter density field is constructed by partitioning the particle masses onto the grid cells using the Triangular Shaped Cloud (TSC) mass assignment scheme. The vorticity field is obtained by the fourth order finite difference of  $\vec{\omega} = \nabla \times \mathbf{v}$  at grid cells in a post simulation procedure.

We first take a look at the density field. While a subtle difference can be found in the dark matter distribution between two codes, the difference in the baryonic gas distribution is significant. The gaseous structures in the WENO sample are more well developed than their counterpart in the TVD sample. Since the WENO code attains high order accuracy,

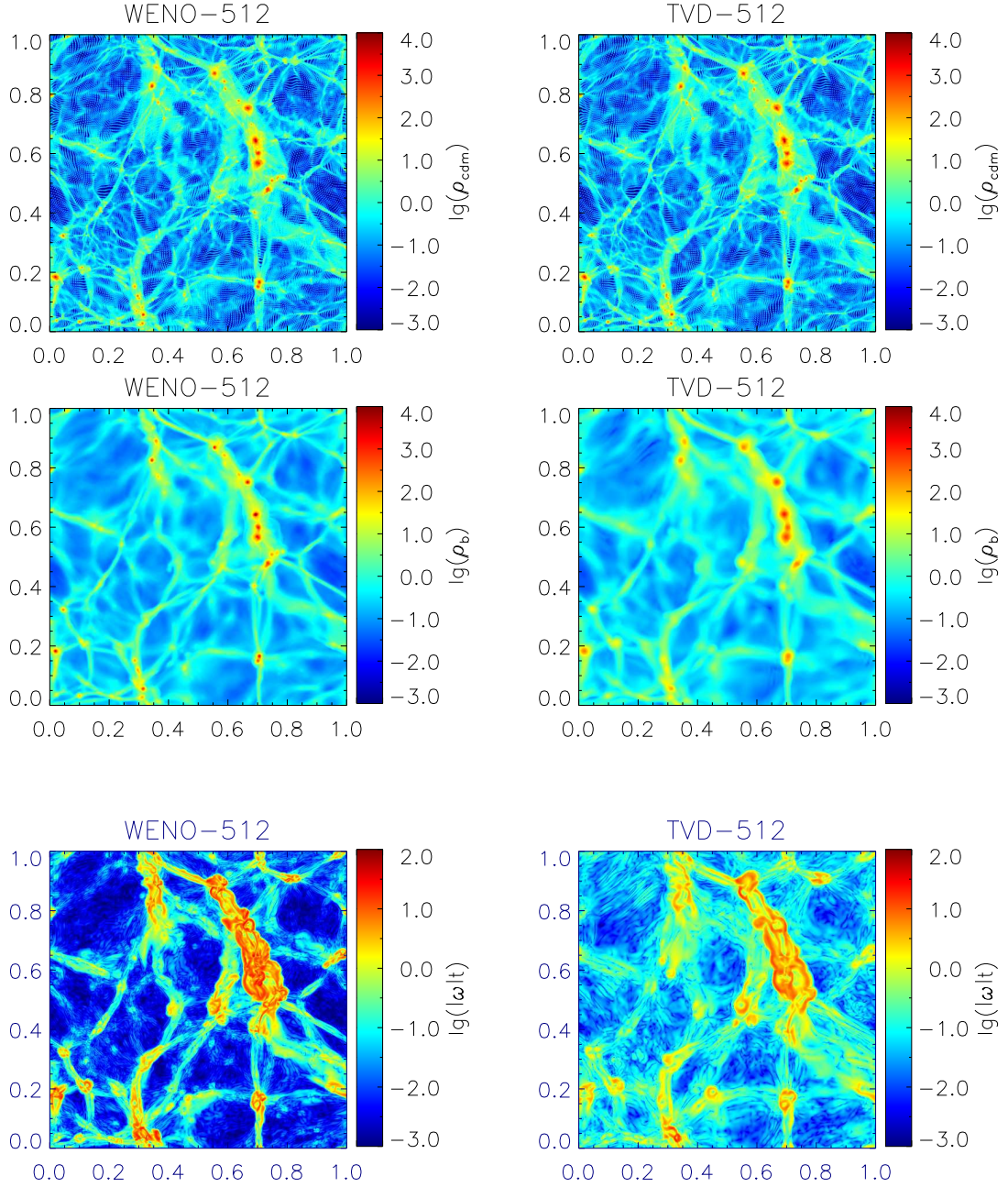


Fig. 1.— Dark and baryonic matter density, in unit of the cosmic mean, and vorticity normalized by cosmic time in a slice of  $25 \times 25 \times 0.25 h^{-3} \text{ Mpc}^3$  in the  $512^3$  simulations at  $z = 0$ . The top (middle) row gives dark (baryonic) matter density, and the bottom row is vorticity. The left (right) column is extracted from the WENO-512 (TVD-512) simulation.



it resolves more sub-structures within the high-density regions. For example, we call the reader’s attention to the gaseous halo located at  $\sim (0.7, 0.2)$ , where two gaseous density peaks are sharply resolved in the WENO sample, however, only a single clumpy core can be found in the TVD sample.

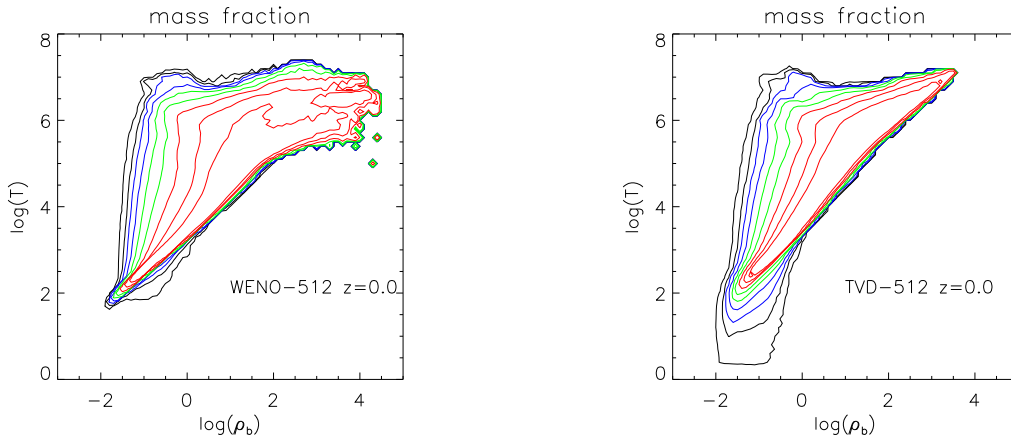


Fig. 2.— Mass distribution as function of gas density and temperature in the  $512^3$  simulations run by the WENO and TVD codes at  $z = 0.0$ . Left: WENO-512. Right: TVD-512.

This trend is shown more clearly by the gas mass fraction distribution in the density-temperature space, as displayed in Fig. 2. Once the normalized over-density exceeds 10, gaseous structures in the WENO-512 run would go through a relatively more rapid growth in density, and slower growth in temperature than the TVD-512 run. This difference may partly result from the different levels of numerical viscosity. The relatively higher numerical viscosity in the TVD scheme could artificially dissipate the kinetic energy associated with both compressible and incompressible motions into thermal energy more effectively, and hence smear out gaseous density transition in the process of structure formation. Despite the different resolution and scope, this is in analogous to the mechanism that Nelson et al. (2013) described, by which the turbulent motions on large scales in the SPH-based Gadget simulation are spuriously dissipated into thermal energy, rather than realistically dissipated by cascading to smaller scales in the AREPO. Consequently, part of the baryonic gas component is locked in the diffuse, hot halos of central galaxies in the SPH code, instead of accreting, cooling and entering into more over-dense central region.

Fig. 1 demonstrates that highly developed vortices also shows filamentary and knotted structures.  $\omega t$  can be as high as  $\sim 100$ , i.e., the turn-over time is about  $1Gyr$  at  $z = 0$ . The difference in the vorticity field between two samples shows a similar trend as in the baryonic matter. Vorticity in the WENO-512 simulation has a higher magnitude and more concentrated configuration. Both the vorticity and baryonic density fluctuation variations

in the TVD-512 sample lag than those in the WENO-512 sample.

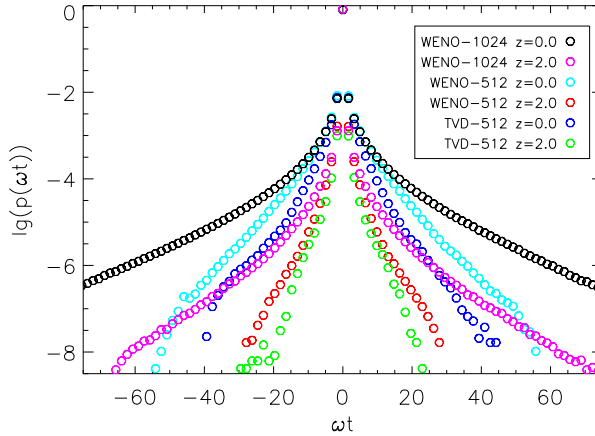


Fig. 3.— Probability distribution function of the normalized vorticity  $\omega t$  in the  $512^3$  and  $1024^3$  simulations run by the WENO and TVD codes at  $z = 2.0, 0.0$ .

The probability distribution functions of vorticity in the  $512^3$  and  $1024^3$  simulations are given in Fig. 3. Long, extended tails are present in the WENO-1024 since  $z = 2$ , confirming the results in ZFF2010. The discrepancy between the WENO and TVD schemes is found to appear earlier than  $z = 2$  and is much more evident at  $z = 0$ . We note that the vorticity in the WENO-512 simulation is under-developed compared to that in ZFF2010, especially for  $\omega t > 20$ , even though the resolution is the same. The difference should be mainly introduced by the different flux splitting methods. The local Lax-Friedrichs method in ZFF2010 bears more dispersion and slightly less dissipation.

### 3.2. Vorticity Power Spectrum and Turbulence-Developed Range

The power spectra of vorticity can be further used to estimate the ranges of spatial scale within which turbulence have been fully developed in the IGM. According to the condition suggested by Batchelor (1959), fully developed turbulence within a given scale range should satisfy the equality in wavenumber space,

$$P_\omega(k) \approx k^2 P_v(k), \quad (2)$$

where  $k$  is the wavenumber,  $P_\omega(k)$  and  $P_v(k)$  are the Fourier power spectra of vorticity and velocity, respectively. Namely, in the regions that turbulence is highly developed, the fluctuating velocity should be dominated by the curl component. In practice, we label the scale range where the margin is less than  $\sim 0.3$  dex as the turbulent scale range.

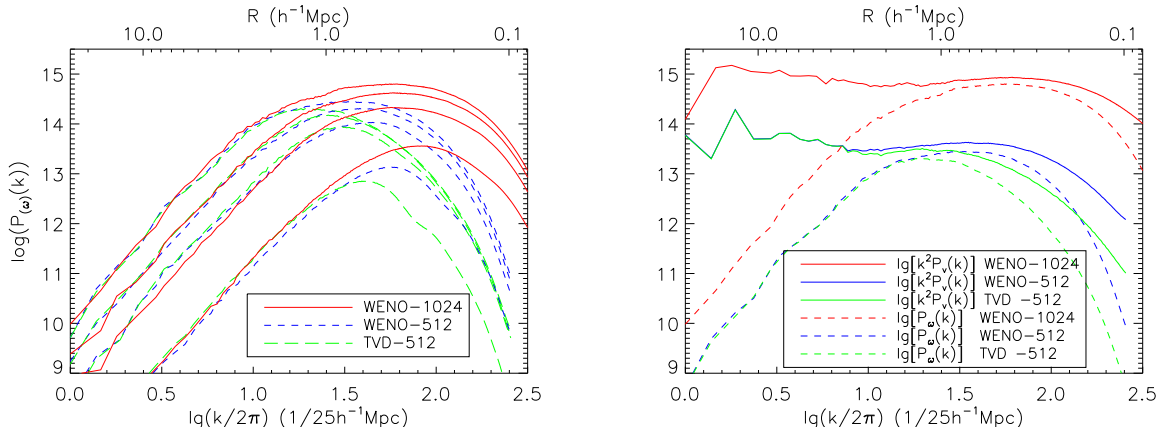


Fig. 4.— Left: Power spectra of vorticity at  $z = 2.0, 1.0, 0.5, 0.0$ , arranged in bottom-up order. Solid, dashed and long dashed lines represent the WENO-1024, WENO-512 and TVD-512 results. Right: Power spectra of velocity and vorticity in the  $512^3$  and  $1024^3$  samples at  $z = 0$ . The lines of the  $512^3$  samples have been shifted down by an order of magnitude for the sake of clarity.

The evolution of vorticity power spectra since  $z = 2$  is given in Fig. 4, which suggests that most of the power is gained between  $z = 2.0$  and  $z = 0.5$ , the same epoch in which the cosmic structure formation activity is the most violent. Both the differences between samples produced by different schemes with the same resolution, and by different resolution with the WENO scheme are very significant under  $\sim 1.0 h^{-1}$  Mpc, and can date back to  $z = 2.0$ . The former could only result from the effect of dissipation by numerical viscosity, and the latter would be caused by the gravity force resolution additionally. The margins keep growing as the scale decreases down to  $\sim 200 h^{-1}$  kpc, and reach about an order of magnitude. Difference can barely be found at scales larger than  $\sim 2 h^{-1}$  Mpc.

In Fig. 4, we also compare the power spectra of velocity and vorticity at  $z = 0.0$ . The turbulence scale range inferred from Eq.(2) are around  $300 h^{-1}\text{kpc} - 2 h^{-1}$  Mpc and  $600 h^{-1}$  kpc  $- 2 h^{-1}$  Mpc in the WENO-512 and TVD-512 samples, respectively. The turbulent range in the WENO-1024 run is about  $\sim 200 h^{-1}$  kpc  $- 2 h^{-1}$  Mpc at  $z = 0$ , which is basically consistent with the result in ZFF2010, although the higher dispersion introduced by the local flux splitting likely have artificially expanded the turbulence range there. Both the total velocity and its curl part in the IGM would be effectively damped if a considerable numerical viscosity exists. Actually, the damping effect of numerical diffusion on the velocity fluctuation has been observed in hydro-only, supersonic turbulence. While the upper end  $l_u$  of the IGM turbulent range is robust, higher numerical viscosity would lead to a larger dissipation scale,  $l_d$ , and hence a shorter turbulent range. Results of the positivity-preserving

WENO schemes in this paper show a much weaker so called bottleneck effect (Kritsuk et al. 2007) near the dissipation scale than in ZFF2010.

### 3.3. Compressive Ratio

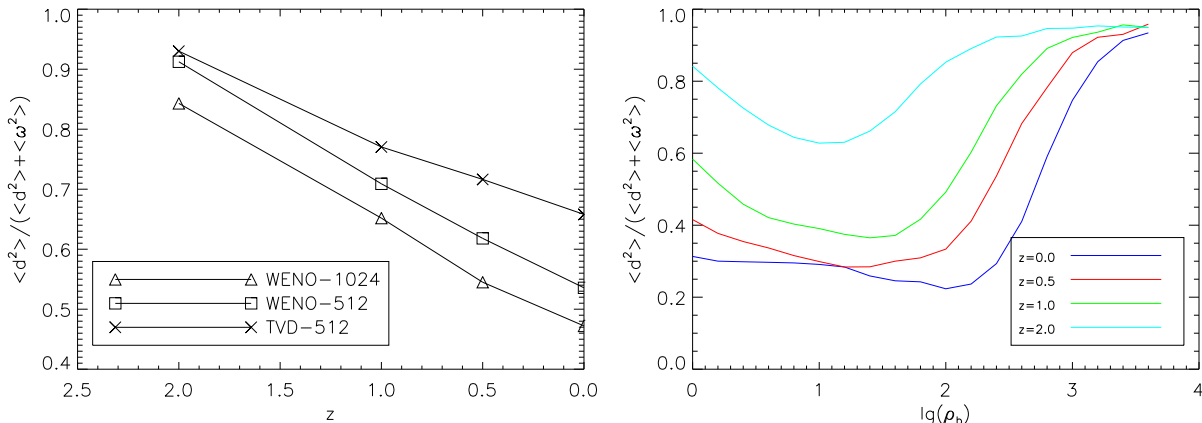


Fig. 5.— Left: Small-scale compressive ratio in the WENO-1024 (triangle), WENO-512 (square) and TVD-512 (cross) simulations since  $z = 2$ . Right: Small-scale compressive ratio in different baryonic density bins in the WENO-1024 simulation.

During the hierarchical structure formation, the motions of the IGM are driven by the curl-free gravity field, and hence are dominated by the compressive mode initially in both the linear and the quasi-linear regimes. The vortical motion, mostly produced by the baroclinity in the post regions of curved shocks, develops rapidly since  $z \sim 2$  and can overwhelm the compressive motion within the turbulence range. To characterize this transition, we investigate the relative importance of the vortical over the compressible motions by the so called small-scale compressive ratio (Kida & Orszag 1992)

$$r_{CS} = \frac{\langle |\nabla \cdot v|^2 \rangle}{\langle |\nabla \cdot v|^2 \rangle + \langle |\nabla \times v|^2 \rangle} = \frac{\langle d^2 \rangle}{\langle d^2 \rangle + \langle \omega^2 \rangle} \quad (3)$$

Fig. 5 gives the small-scale compressive ratio  $r_{CS}$  in the  $512^3$  and  $1024^3$  simulations. The vortical motion undergoes a dramatic growth at  $z < 2$ , and is comparable to the compressive motion in the  $1024^3$  simulation at  $z = 0.0$ , Consequently  $r_{CS}$  drops from 0.84 to 0.47 during this period. The magnitude of  $r_{CS}$  at  $z = 0$  is close to the compressively driven isothermal turbulence with root mean square Mach number  $\simeq 2.5$  in Schmidt et al(2009), and higher than the time-averaged value, 0.28, for the isothermal turbulence with Mach

number  $M \simeq 6.0$  in Kritsuk et al (2007). Lower resolution and relatively higher numerical viscosity attenuate this transition and result in relatively higher compressive ratio.  $r_{CS}$  is about 0.66 at  $z = 0$ . in the TVD-512 sample, suggesting the motion of the IGM is still dominated by the compressive mode.

We calculate  $r_{CS}$  in different gas density bins in the  $1024^3$  simulation, which is also presented in Fig. 5. In regions with baryonic density  $\rho_b \lesssim 10^3$ , the vortical motion grows rapidly since  $z = 2.0$ . For  $\rho_b \lesssim 10^2$ , the curl velocity can overwhelm the compressive part as early as  $z = 1.0$ . Moreover,  $r_{CS}$  can be as low as 0.2 for  $\rho_b \simeq 100$  at  $z = 0.0$ . Comparing with the compressive motions, the vortical motion grows more rapidly before entering into outskirts of clusters, i.e,  $\rho_b \sim 100$ , In the clusters and their outskirts, the vortical motion may dissipate faster than the compressive motions. The magnitude of  $r_{cs}$  here is volume weighted, which would be significantly higher than the corresponding mass-weighted. The discrepancy in Schmidt et al.(2009) is around  $0.2 \sim 0.3$  *dex*, comparable with the difference between our results and the mass weighted value in Iapichino et al.(2011).

#### 4. Properties of Curl and Compressive Velocity

In this section, we focus on the two components of the velocity field of the IGM,  $\vec{V}$ , which can be separated by the Helmholtz-Hodge decomposition (Ryu et al. 2008; Sagaut & Cambon et al. 2008).

$$\vec{V} = \vec{V}_{curl} + \vec{V}_{div} + \vec{V}_{unif} \quad (4)$$

where,  $\vec{V}_{curl}$  is the divergence-free curl velocity associated with the vorticity,  $\nabla \cdot \vec{V}_{curl} = 0$  and  $\nabla \times \vec{V}_{curl} = \nabla \times \vec{V}$ ;  $\vec{V}_{div}$  is the curl-free component,  $\nabla \times \vec{V}_{div} = 0$  and  $\nabla \cdot \vec{V}_{div} = \nabla \cdot \vec{V}$ . The curl-free component  $\vec{V}_{div}$  represents the compressive velocity. The remaining component  $\vec{V}_{unif}$  is both curl-free and divergence-free, which is actually negligible in the simulation.

##### 4.1. Curl Velocity Distribution

As an example, Fig. 6 shows the velocity field and its curl component projected over the gas density in the WENO-512 sample in the same slice as Fig.1. The curl velocity is basically associated with the high vorticity region, consistent with the definition above. The maximum curl velocity in the slice is  $150km/s$ , relative to  $200km/s$  for the total velocity.

The mean curl velocity as function of gas density,  $\bar{V}_{curl}(\rho_b)$ , and temperature,  $\bar{V}_{curl}(T)$  from  $z = 2.0$  to  $z = 0.0$  are presented in Fig. 7. We focus on the region with  $\rho_b > 1.0$ , where the vorticity and curl velocity are well developed. Correspondingly, the temperature is

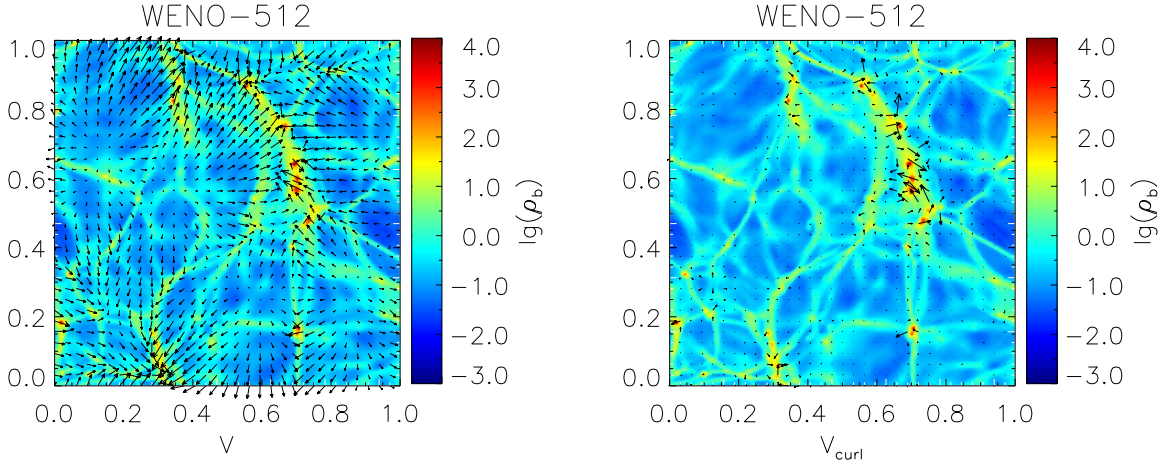


Fig. 6.— Velocity field and its curl component of the IGM projected over gas density in the same slice as in Fig.1 at  $z=0$ , extracted from the WENO-512 sample. The maximum velocity and curl velocity are around  $200\text{km/s}$  and  $150\text{km/s}$  in this slice.

generally higher than  $10^4 K$ , as shown in Fig. 2. Both the magnitude and trends are almost the same in all the simulations. A discrepancy of a few  $\text{km/s}$  exists all through the range. As a very small fraction of cells has gas density  $\rho_b > 3 \times 10^3$  in the TVD samples, comparison is not available there. Starting at a level of  $10\text{km/s}$  at low density or temperature, the magnitude of  $\vec{V}_{curl}$  grows rapidly till  $\rho_b \sim 30$ , or  $T \sim 10^6 k$ , reaches  $\simeq 90\text{km/s}$  and flattens out henceforth at  $z = 0.0$ . Fig. 7a, also shows our approximation at  $z=0$  as the black solid line, given

$$V_{curl}(\rho_b) = 10.0 \times \exp\{-[\lg(\rho_b/100.0)]^2\} + 85.0 \times \exp\{-[\lg(\rho_b/\rho_c)/2]^2\} \text{ km/s}, \quad (5)$$

where,  $\rho_c = 200.0/\Omega_m$ .

The magnitude in highly over-dense clusters in our simulation is below the weak constraints placed by direct or indirect observation methods, i.e,  $\simeq 200 \sim 1000\text{km/s}$ (Sanders et al. 2010, 2011,2013). The absence of recipes dealing with star formation, magnetic fields and AGN in our simulation may underestimate the turbulent motion in clusters. The level of  $10 \sim 20\text{km/s}$  at  $z = 2.0$  is also lower than the turbulent line broadening in Zheng et al.(2004) at  $z \simeq 2.7$  by a factor of  $\simeq 2$ . In Oppenheimer & Dave (2009), the density-dependent sub-resolution turbulent velocity added by hand are  $b_{turb} = 13, 22, 40$  and  $51 \text{ kms}^{-1}$  for  $\rho_b = 20, 32, 100$  and  $320$  at  $z = 0.25$ , in order to match the O VI absorbers in simulation with observation. The assumed relation between turbulence velocity and density is supposed to follow the fitting formula  $v_{turb} = 13.93\log(n_H) + 101.8\text{kms}^{-1}$ , for  $n_H = 10^{-4.5} - 10^{-3.0} \text{cm}^{-3}$ . Their magnitude is lower than our results in the  $1024^3$  simulation by  $\sim 15 \text{ kms}^{-1}$ .

The observed tendency of curl velocity in all the samples would have been affected by the

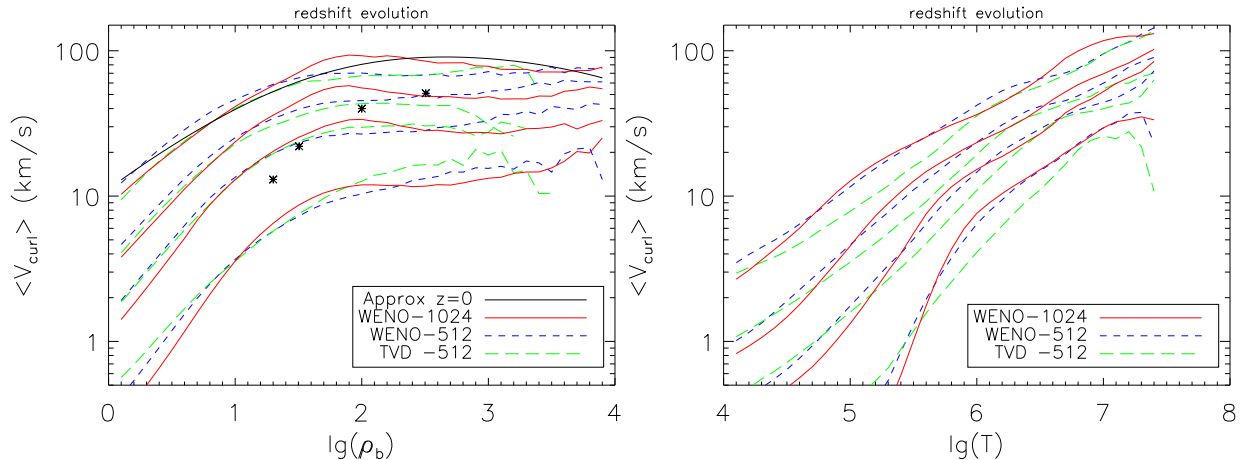


Fig. 7.— The curl velocity as function of gas density (left), and temperature (right). Lines of  $z = 2.0, 1.0, 0.5, 0.0$  are in bottom-up order. The black solid line in the left panel indicates the approximation at  $z=0$ . Asterisks indicate the un-resolved sub-grid turbulent velocity added by hand in OD09 at  $z = 0.25$ .

UV background, structure formation history and dissipation simultaneously. Re-ionization by the UV background will enhance the thermal energies in our simulations and heat the gas in the low density regions and damp the pressure fluctuations. Once entering into the nonlinear regimes, the violent accretion of gas onto sheets and filaments will effectively produce shocks and vorticity, and hence the curl velocity. Virial relaxation will make the vorticity decay in the highly nonlinear regimes and flatten the curl velocity function.

As has been shown in Fig.2, there is a notably larger fraction of gases located in the high density regions in the WENO-512 samples. Difference in the total kinetic turbulent energy between two codes is considerable, as  $\bar{V}_{curl}(\rho_b)$  is about the same. Rather than cascading into small scales, a substantial part of the kinetic turbulent energy in the TVD-512 samples may have been dissipated into thermal energy by numerical viscosity during cosmic structure formation.

#### 4.2. Curl and Compressive Velocity Power Spectra

For the fully developed turbulence in incompressible fluids, the velocity power spectra follow the well known Kolmogorov law as  $P_v(k) \sim k^{-5/3}$  in the inertial range. Since the early 1990s, two- and three-dimensional high resolution simulations of both forced and decaying supersonic turbulence in the fields of hydrodynamic and interstellar medium, however, show that the power index of the velocity power spectra deviates from  $-5/3$ . A  $k^{-2}$  power law

is obtained in both mildly and highly compressible turbulence (Porter et al. 1992, 1998; Kritsuk et al. 2007, Federrath et al. 2010), and is close to the Burgers scaling.

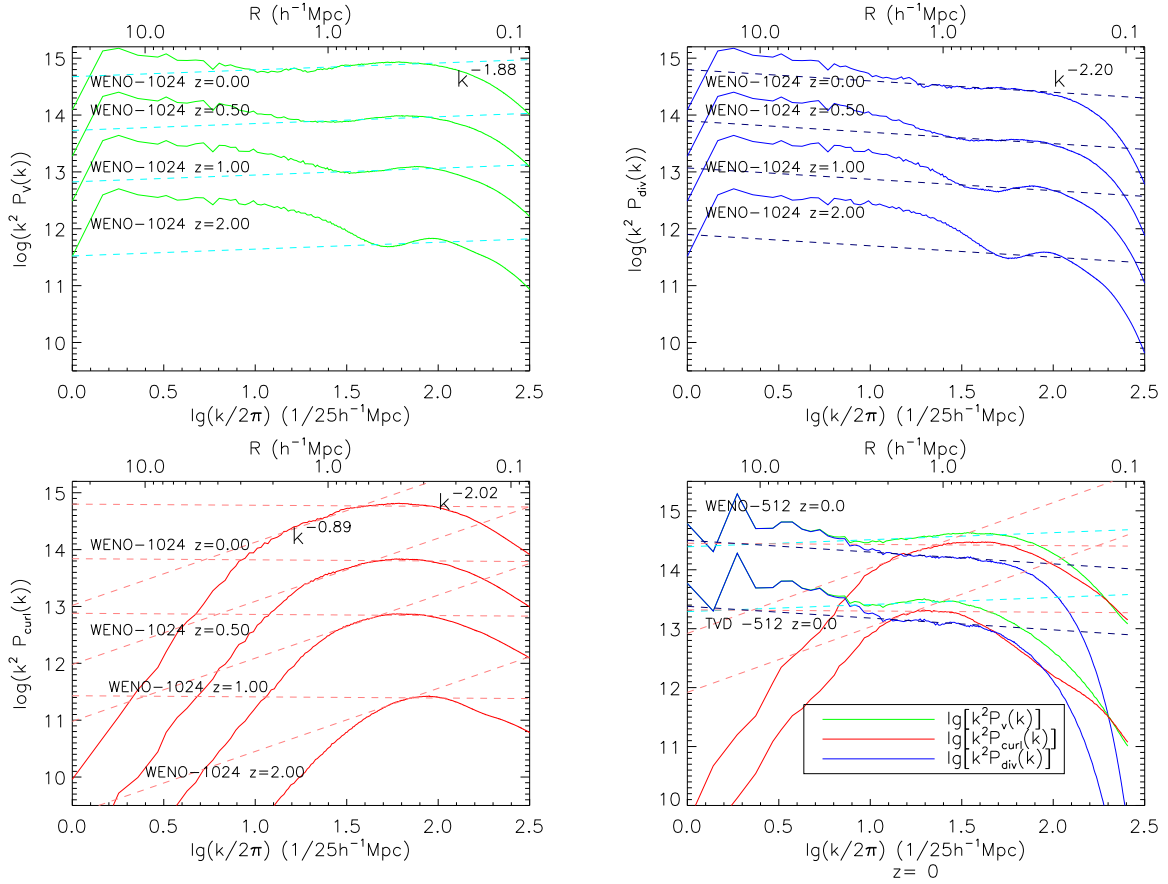


Fig. 8.— Compensated power spectra of velocity (top left), and its compressible (top right) and curl (bottom left) components in the WENO-1024 simulation at  $z = 2.0, 1.0, 0.5, 0.0$ , arranged in bottom-up order in each panel. Lines of  $z = 0.5, 1.0, 2.0$  have been shifted down by 0.5, 1.0, 1.5 dex respectively for the sake of clarity. Bottom right: Results of the WENO-512 and TVD-512 samples at  $z = 0$ . Dashed straight lines are the fitted power law.

Fig.8 displays the compensated power spectra of flow velocity,  $k^2 P_v(k)$  (upper left), and the curl,  $k^2 P_{v,curl}(k)$  (lower left) as well as the compressive components  $k^2 P_{v,div}(k)$  (upper right) measured in our highest resolution run, WENO-1024. Clearly,  $k^2 P_{v,curl}(k)$  overwhelms  $k^2 P_{v,div}(k)$  in the inertial range of fully developed turbulence identified by Eqn.(2). At  $z = 0$ , the velocity power spectra is found to be well fitted by  $k^{-1.88}$  within the turbulence range. Actually, this scaling behavior was established as early as  $z = 1.0$ . Similarly, the power spectra of the compressible velocity follows a scaling law of  $k^{-2.20}$  in the same range. While for the curl velocity, the scaling behavior shows a transition from  $k^{-0.89}$  to  $k^{-2.02}$ . The



transition scale  $l_t$  grows along with the development of turbulence, namely, grows with the cosmic time as the upper-end scale,  $l_u$ , does. For instance, for the WENO-1024 simulation,  $l_t$  is about  $0.32h^{-1}Mpc$  at  $z = 2$ . and goes up to  $0.68h^{-1}Mpc$  at  $z = 0$ . Meanwhile, the range for the fully developed turbulence is enlarged from  $0.2 \sim 0.6h^{-1}Mpc$  at  $z = 2$  to  $0.2 \sim 2.0h^{-1}Mpc$  at  $z = 0$ . The same scaling law is also justified in the  $512^3$  samples, but the dissipation scale,  $l_d$ , is found to be a little bit larger than the WENO-1024 samples due to the numerical viscosity. For the WENO-512, it is about  $0.3h^{-1}Mpc$ . The  $512^3$  samples follow the same scaling law in their shortened turbulence inertial range, with  $l_t$  is enlarged as  $l_d$  does due to numerical viscosity.

The scaling law of the velocity power spectrum in our samples indicates that the turbulence in the IGM is more likely following the Burgers turbulence scaling between  $l_t$  and  $l_d$ , consistent with results in previous works of supersonic isotropic turbulence (Porter et al. 1992, 1998; Kritsuk et al. 2007, Federrath et al. 2010). This range would correspond to the supersonic phase, as proposed by Porter et al. (1992, 1994), where both the curl and compressive velocity power spectra follow  $\sim k^{-2}$ . During this phase, the vorticity can be effectively produced by the baroclinity term, as shocks form and interact with each other. The error introduced by the bottleneck effect, of which more details can be found in Kritsuk et al. 2007, is about 0.05 in the power index of the total velocity spectrum.

On the other hand, the velocity field in the turbulence range between the transition scale,  $l_t$ , and the upper-end scale,  $l_u$ , exhibits a similar scaling as the post-supersonic phase in Porter et al. (1992, 1994), where the compressive velocity component still follows a  $\sim k^{-2}$  law while the curl velocity follows a  $\sim k^{-1}$  law. The vorticity evolution in this phase is subject to subsonic vorticity dynamics, dominated by vortex interaction and decay, although shocks are still active. In summary, turbulence in the IGM may possess two different phases simultaneously.

### 4.3. Turbulent Pressure Support and Baryon Fraction

The vortical motions would provide a non-thermal turbulent pressure during gravitational collapse (Chandrasekhar 1951a, 1951b). Ryu et al. (2008) used the kinetic energy associated with vortices,  $\rho V_{curl}^2/2$ , to estimate the kinetic turbulent energy in the IGM. The turbulence pressure support is then measured by the ratio of  $\varepsilon_{tur} \sim \rho V_{curl}^2/2$  to the internal thermal energy,  $\varepsilon_{int}$ . Fig. 9 shows the mass weighted mean non-thermal support ratio as function of gas density,  $\langle \varepsilon_{tur}/\varepsilon_{int}(\rho_b) \rangle$ , and temperature,  $\langle \varepsilon_{tur}/\varepsilon_{int}(T) \rangle$  at different redshifts in our simulations. The trends with increasing temperature and density, and the evolution with decreasing redshift are almost the same in different samples.

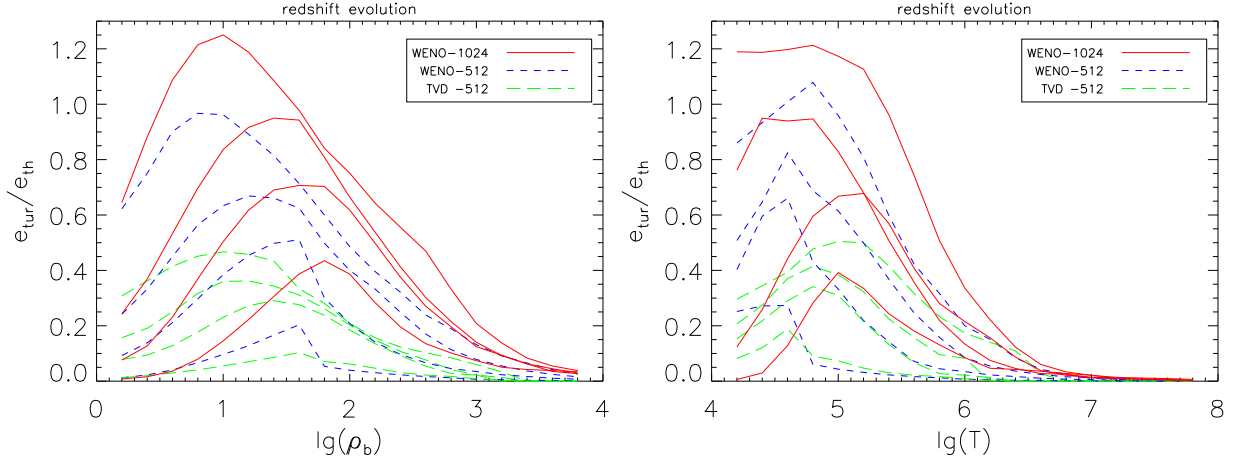


Fig. 9.— The ratio of kinetic turbulent energy to thermal energy as function of gas density (left) and temperature (right). Lines of  $z = 2.0, 1.0, 0.5, 0.0$  are in bottom-up order.

For the same resolution, the ratio in the WENO-512 sample is significantly higher than the TVD-512 sample, and is close to 1.0 for  $\rho_b \simeq 10$ , or  $T \simeq 10^5 K$  at  $z = 0$ . This result is actually in agreement with the curl velocity distribution  $\bar{V}_{curl}(\rho_b)$  and  $\bar{V}_{curl}(T)$ . As shown in Fig.2, the baryonic mass fraction in the  $\rho_b - T$  phase diagram varies much between the WENO and TVD simulations. For overdense regions  $\rho_b > 1.0$ , the mass weighted mean temperature,  $\bar{T}(\rho_b)$  in the WENO-512 sample is lower, namely, the thermal energy density  $\varepsilon_{int} \sim \rho \bar{T}(\rho_b)$  is also lower. Since  $\varepsilon_{tur} \sim \rho_b \bar{V}_{curl}^2(\rho_b)$  are comparable in two codes, consequently, the ratio of  $\varepsilon_{int}/\varepsilon_{tur}$  in the WENO-512 sample is getting higher.

The mean ratio as a function of temperature is more complicated. In the range of  $10^4 - 10^5 K$ , the mass distribution at a given temperature,  $f(\rho_b, T)$ , does not vary much between two codes. Higher  $\langle \varepsilon_{tur}/\varepsilon_{int}(T) \rangle$  in the WENO-512 results from higher  $\langle \varepsilon_{tur}/\varepsilon_{int}(\rho_b) \rangle$  for  $\rho_b = 1.0 - 10^4$ . For  $T > 10^5 K$ , the mean density,  $\bar{\rho}_b(T)$ , in the WENO-512 is shifted to higher density region comparing to the TVD-512, and is generally larger than tens of the cosmic mean. On the other hand,  $\varepsilon_{tur}/\varepsilon_{int}$  decreases as the gas density increases for  $\rho_b > 10$  in both codes. Consequently, the margins in  $\langle \varepsilon_{tur}/\varepsilon_{int}(T) \rangle$  between the WENO-512 and TVD-512 simulations peak at around  $10^5 K$ , depending on the redshift, and would decrease toward higher temperature.

In the reference run WENO-1024, the non-thermal pressure support is substantially stronger than the WENO-512 sample, and is comparable to the thermal pressure for  $\rho_b \simeq 10 \sim 100$ , or  $T < 10^{5.5} K$  at  $z = 0.0$ . The kinetic turbulent energy ratios as a function of temperature obtained here are different from Ryu et al. (2008) at  $T < 10^{4.5} K$ . More specifically, the ratio grows rapidly as the temperature decrease at  $T < 10^{4.5} K$  in Ryu et al.(2008). Meanwhile, the magnitude there is larger than ours by about 0.2 dex. These

differences should mainly result from the UV background, which is not included in Ryu et al. (2008). The UV background would enhance the temperature of gas and might smear out pressure fluctuations and hence the baroclinity outside of clusters. In addition, the magnetic field included in Ryu et al.(2008) might amplify the turbulent motion in the IGM.

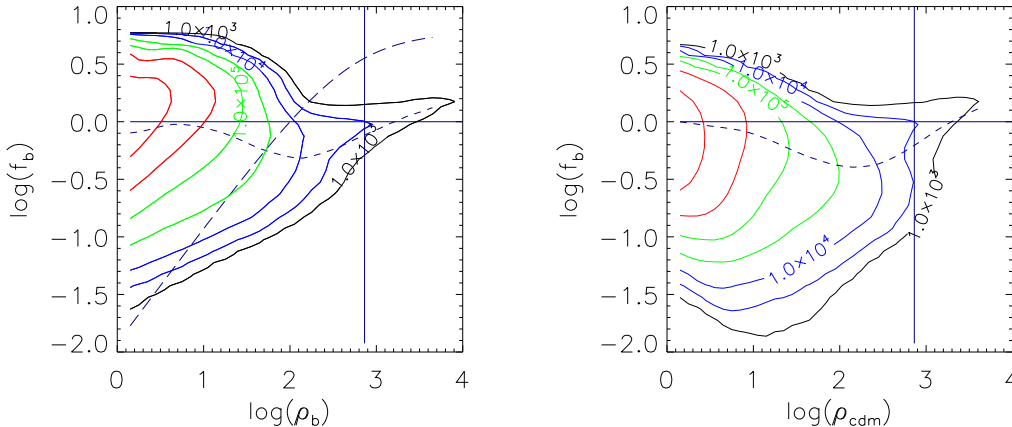


Fig. 10.— Left (right) panel shows contours of cell-counting in the phase space of baryonic (dark) matter density and normalized baryon fraction in the WENO-1024 sample at  $z = 0.0$ . Short dashed lines are the averaged baryon fraction  $\bar{f}_b(\rho_b)$  ( $\bar{f}_b(\rho_{cdm})$ ) in different density bins. Long dashed lines in the left panel indicate a constant dark matter density of 100.0.

Turbulence pressure of the IGM may cause both the density and velocity fields of baryonic gas to be different from those of underlying collisionless dark matter, result in the baryon fraction deviating from the cosmic mean  $F_b^{\text{cosmic}}$  (Zhu, Feng, Fang 2011). Fig.10 shows the contours of cell numbers in the space of normalized baryon fraction  $f_b$  and gas density drawn from the 1024<sup>3</sup> simulation at  $z = 0.0$ . Both the gas and dark matter density at grid cells are smoothed with a radius of one grid cell, and then used to calculate the baryon fraction. A considerable volume of the cells does deviate from the cosmic mean, and shows significant scatter.

The baryon fraction in different gas density bins, shown as the short dash line in the left panel of Fig.10, suggests that the maximum deviation lies in  $\rho_b \sim 100$ , coincidentally overlapping with the range that the maximum turbulence pressure support and lowest compressive ratio takes place. Contours in the dark matter density space are also presented in Fig. 10. The deviation is much more significant and no longer follow a simple linear function of  $f_b(\rho_b)$ , which can be illustrated by the long dashed line that represents a constant dark matter density 100 in the left panel. In the outskirts of clusters, and halos with size close to one grid cell, the baryon fraction is around 0.4 – 0.55. However, in the central regions of clusters with smoothed density  $> 10^3$ , the baryon fraction is larger than the cosmic mean,

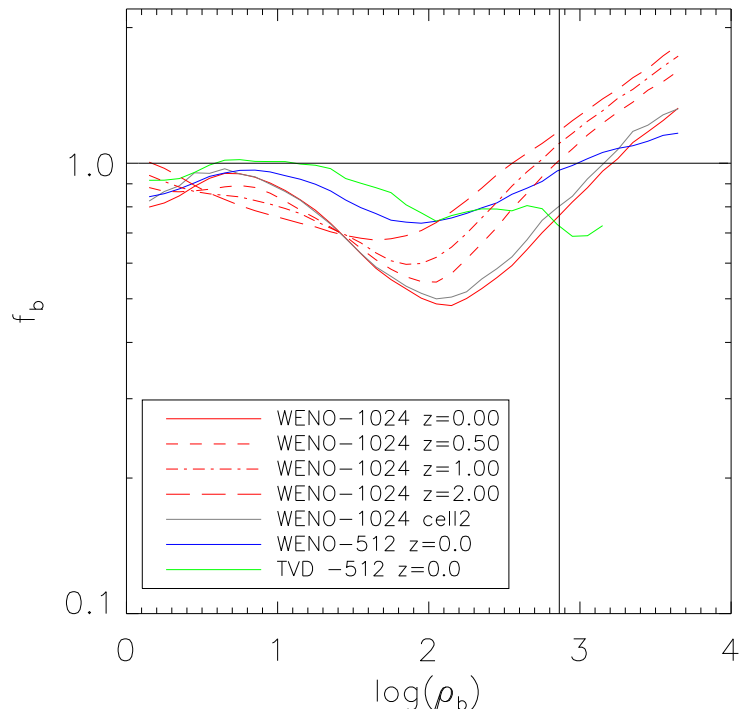


Fig. 11.— Averaged baryon fraction  $\bar{f}_b(\rho_b)$  as a function of baryonic matter density in the  $1024^3$  and  $512^3$  simulations. The cell2 represents averaged baryon fraction in cubic boxes of side length of two grid cells.

suggesting feedback from star formation may be needed. For halos whose sizes are larger than a couple of grid cells, the total baryon fraction would be some value between those in the central and outer regions.

Fig.11 gives the evolution of the baryon fraction in different gas density bins since  $z = 2$ . While the deviation in the range of  $10 < \rho_b < 10^3$  is amplified with time, the discrepancy in the central region is gradually reconciled. The deviation in the  $1024^3$  sample, calculated in cubic boxes of side length of two grid cells, i.e., equal to the size of one grid cell in the  $512^3$  samples, overwhelms results in the  $512^3$  simulation at  $z = 0$ , except for the cluster region in the TVD run. A possible explanation is that the compressive motions in the TVD simulation have been effectively dissipated by the numerical viscosity, rather than cascading into small scales and accreting on to higher density structures.

In summary, the baryon fraction in the IGM significantly deviates from the cosmic mean in our simulations. The deviation shows a preliminary positive correlation with the turbulence pressure support. The case in virialized halos is much more complicated, and demands

more careful investigation. However, small halos are more likely to suffer from baryon deficit. Its link with the baryon missing in dwarf galaxies may require more extensive investigation, especially need to consider the impact of radiative, thermal and kinetic feedback.

## 5. Properties of Shocks

The shocks formed during the hierarchical structure formation can effectively produce vorticity via the baroclinity term (Kida & Orszag 1990; Ryu et al. 2008; ZFF2010), and hence play an important role in injecting turbulence into the IGM. Relatively higher numerical viscosity would smear out shocks more significantly, and consequently may result in less intensive turbulence. In this section, we investigate the properties of shocks in our simulation samples of  $512^3$  produced by the WENO and TVD schemes. Results from the  $1024^3$  simulation are not included as we intend to study the isolated effect of numerical viscosity. The impact of grid cell size and force resolution on the shocks can be found in Vazza et al. (2009, 2011).

We detect shocks in our samples in a post-simulation way based on the conventional method in Miniati et al. (2000) and Ryu et al. (2003), in which three requirements should be fulfilled to tag a grid cell as shocked region,

- (1)  $\nabla P \cdot \nabla S > 0$
- (2)  $\nabla \cdot V < 0$
- (3)  $|\Delta \log(T)| > 0.11$

A shock is typically resolved by two or three grid cells and its center is defined as the cell that has the minimum  $\nabla \cdot V$ . The mach number of a shock  $M$  is obtained according to

$$\frac{\rho_2}{\rho_1} = \frac{4M^2}{M^2 + 3} \quad (6)$$

$$\frac{T_2}{T_1} = \frac{(5M^2 - 1)(M^2 + 3)}{16M^2} \quad (7)$$

for gas with  $\gamma = 5/3$ , and the subscripts 1 and 2 denote for the pre-shock and post-shock regions, respectively (Landau & Lifshitz 1959).

The third condition in shock detection,  $|\Delta \log(T)| > 0.11$ , corresponds to a Mach number of 1.3. We add one more condition, the density jump over a shock with Mach number 1.3, i.e.,  $\rho_2/\rho_1 > 1.4$ , to prevent overestimating the number of low Mach number shocks by the temperature conditions (Vazza et al. 2009), and exclude pressure jumps that might be caused by errors in calculating internal energy. The shock detection procedure is performed in a one-dimensional way according to the above criterion along three different Cartesian axes. As

Skillman et al. (2008) had shown that, this one-dimensional shock-finding algorithm would over-estimate the number of shocks weaker than  $M \sim 10$  by a factor of  $\sim 3$ . The number of low Mach number shocks found in the two samples, WENO-512 and TVD-512, will both suffer from this limitation, while the discrepancies between the samples are expected to be systematic. Fig. 12 illustrates the shock fronts identified in the same slice shown in Fig. 1. The skeleton of distributions is almost the same in two samples, but the WENO-512 run produces more shocks surrounding the sheets, filaments and compact gas halos. We also present the baroclinity term within this slice. The spacial pattern of the baroclinity term is well confined by shocks and resembles the vorticity shown in Fig.1.

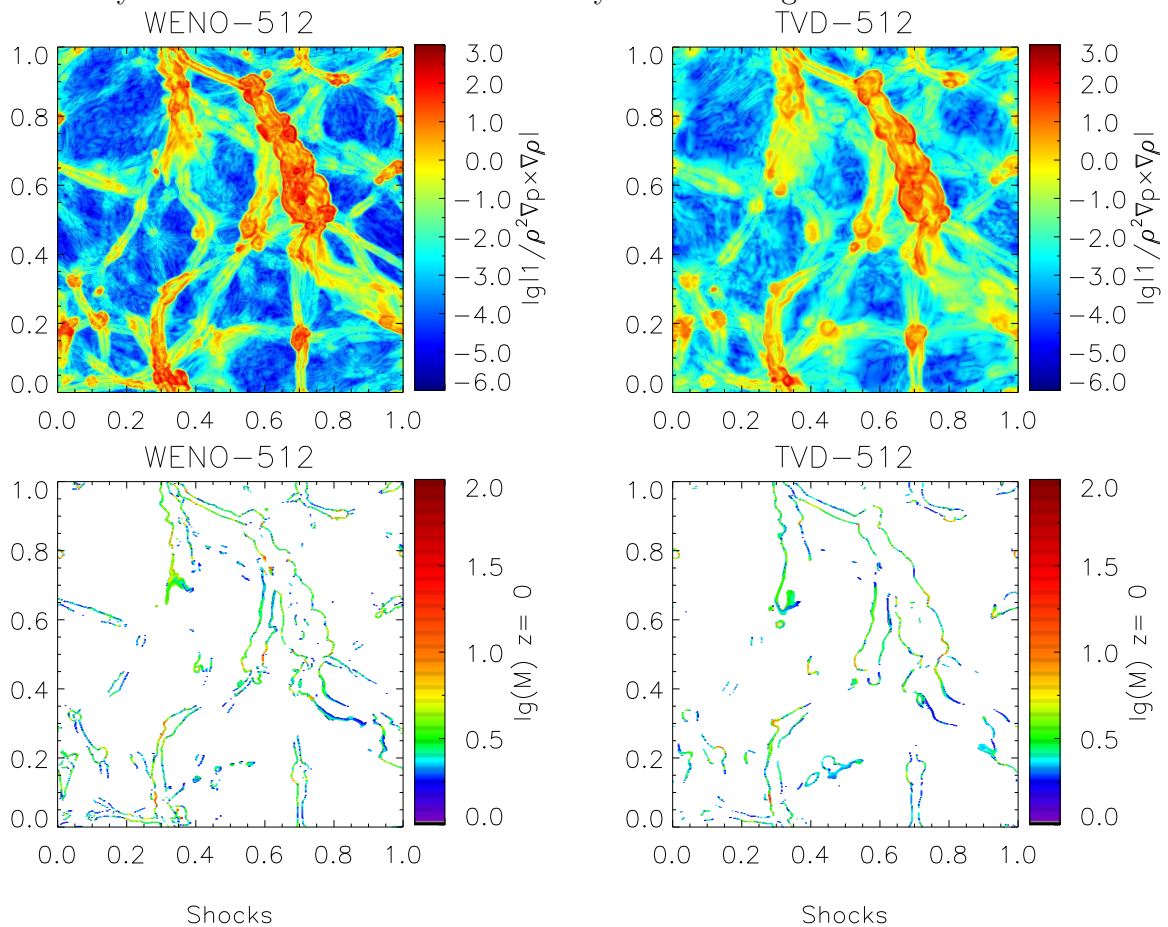


Fig. 12.— Top (bottom) row: Baroclinity (shocks) in the same slice as in Fig. 1. Left (right) column: WENO-512 (TVD-512).

Cosmic shocks are driven by the accretion of gas into sheets, filaments and clusters, and merging between gaseous haloes. As shocks are the sources of vorticity and turbulent velocity, the distribution of shocks in different structure patterns may give us more information about how the vorticity and turbulent motion are damped by numerical viscosity. We report the

details of shock distribution in the following subsections.

### 5.1. External and Internal Shocks

Depending on whether the pre-shock gas is previously shocked or not, shocks in the simulations can be divided into two categories, the external and internal shocks. In practice, shocks with  $T_1 < 10^4 K$  are called the external shocks and vice versa (Miniati et al. 2001; Ryu et al. 2003; Kang et al. 2007). External shocks are formed when unshocked, low-density gas accretes onto nonlinear structures, such as sheets, filaments and knots. Internal shocks are distributed within the regions bounded by external shocks. The internal shocks are produced by: (1) gas infalling from sheets to filaments and knots, and from filaments to knots, (2) gaseous halos merging with each other.

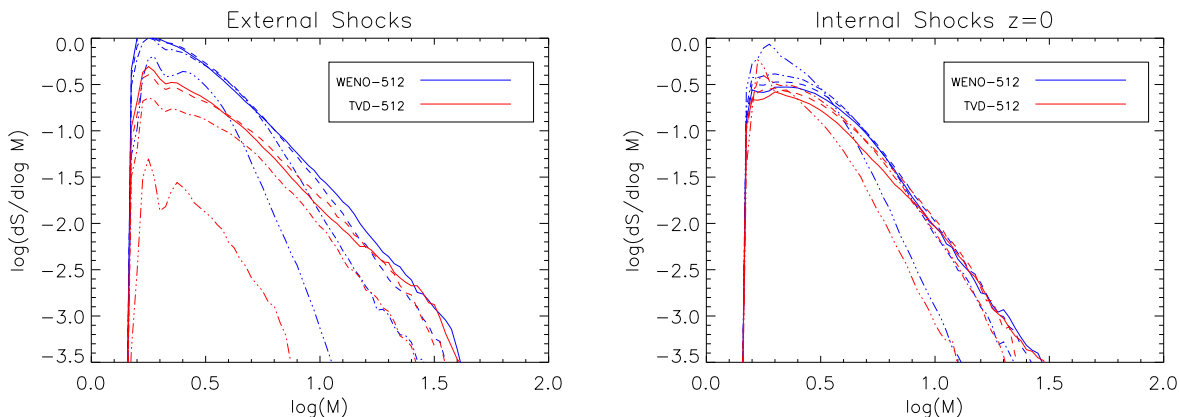


Fig. 13.— Surface area of external and internal shocks in  $512^3$  simulations. Blue lines: WENO-512. Red lines: TVD-512. Solid (dash, dash-dotted, dash-triple-dotted) lines are the results at different redshifts  $z = 0, 0.5, 1.0, 2.0$ .

Fig.13 compares the frequency of external and internal shocks between two codes, measured by the surface area of shocks in logarithmic Mach number bin,  $dS(M, z)/d\log M$  which was firstly proposed in Miniati et al. (2000) and indicates the inverse of distance between shocks. The most striking feature in Fig. 13, is the significant difference in the frequency of external shocks between two codes. Many more external shocks are developed in the WENO-512 simulation from  $z = 2$  to  $z = 0$ , while moderately more internal shocks are formed only at  $z = 2$ . Numerical viscosity has smeared out many shocks in the low density regions in the TVD codes.

Comparing with the result in Ryu et al. (2003), the distribution of external shocks

here have shallower tails over  $M > 10$ , while the distribution of internal shocks is more extended. The former should be mainly due to the UV background and the latter results from the improvement of simulation resolution,  $47.7h^{-1}kpc$  here versus  $97.7h^{-1}kpc$  in Ryu et al.(2003). The number of external and internal shocks weaker than  $M \sim 10$  in our TVD-512 run are consistent with Ryu et al.(2003), which should be significantly over-predicted in comparison with results by the coordinate unsplit algorithm proposed in Skillman et al.(2008)(see their Fig. 4).

## 5.2. Shocks in Various Cosmic Structures

The shock distribution in various cosmic environments can be addressed more explicitly according to either the gas or the total matter density at shock centers. Skillman et al.(2008) and Vazza et al.(2009) studied the shock distributions for varying pre-shock gas density or total matter density, and their redshift evolution. Here, similar to Vazza et al. (2009), we divide the structures that shocks are embedded into four categories according to the total density,

- (1)  $\rho_t = \rho_b + \rho_{cdm} < 6\rho_{crit}$ : voids and under-dense region
- (2)  $6 < \rho_t/\rho_{crit} < 36$ : sheets and filaments
- (3)  $36 < \rho_t/\rho_{crit} < 200$ : outskirts of clusters
- (4)  $\rho_t/\rho_{crit} > 200$ : virialized clusters

where,  $\rho_t$ ,  $\rho_{cdm}$ , and  $\rho_{crit}$  are the total, dark matter and critical density respectively. The boundaries, 6, 36, 200, are slightly different from those in Vazza et al. (2009), and are identical to the mean density of sheets, filaments and halos predicted in Shen et al. (2006).

Fig.14 plots the distribution of shocks in the four types of cosmic structures from  $z = 2.0$  to  $z = 0.0$ . The general trends with decreasing redshifts are identical in two codes: more shocks keep appearing in the under-dense region where the gas keeps accreting to nonlinear structures; more high Mach number and less low Mach number shocks are being developed within the sheets and filaments; the frequency of shocks in clusters and their outskirts, however, is not changed much.

On the other hand, the difference between the WENO-512 and TVD-512 simulations takes place in different structures at different redshifts. At the redshift  $z = 2$ , the shocks in the under-dense region are less developed due to the damping of velocity and density fluctuations by the higher numerical viscosity in the TVD code. Notable difference remains in the under-dense region at  $z = 1$ . Moderate discrepancies exist in all the structures at  $z = 0.5$ . More shocks are formed within the sheets, filaments and outskirts of clusters in the



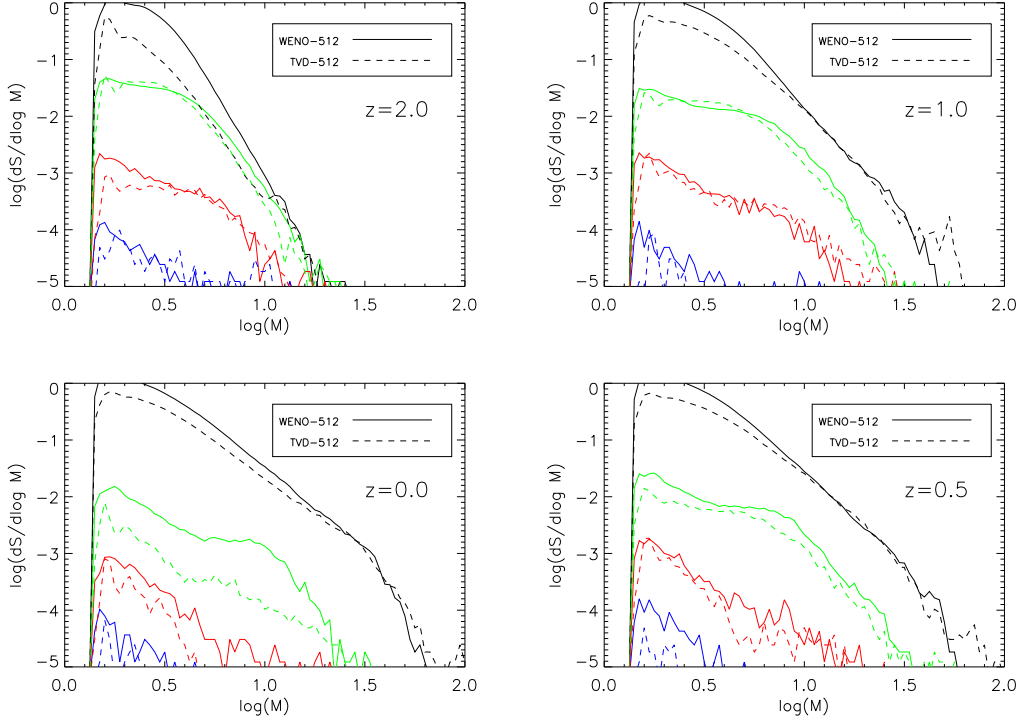


Fig. 14.— Surface area of shocks in various structures in the simulated samples at  $z = 2.0, 1.0, 0.5, 0.0$  (Arranged in clockwise direction). Solid (dotted) lines indicate the WENO-512 (TVD-512) result. Pairs of lines indicate shocks in voids, filaments, outskirts of clusters and clusters from top to bottom.

WENO-512 run at  $z = 0$ .

The majority of shocks in our samples are hosted in low-density regions including voids and filaments, which is in general agreement with Skillman et al.(2008) and Vazza et al(2009). Again, the frequencies of low Mach number shocks are much higher than Skillman et al(2008), by a factor of  $3 \sim 10$ , in all kinds of structures, which may mainly result from the different shock detecting methods. The number distribution of shocks as a function of Mach number became shallower when moving towards dense environment for  $M > 3$  in our simulations, which is contradict with Vazza et al.(2009). The evolution in Skillman et al.(2008), however, is much more complicated. To answer whether this discrepancy is merely brought by the selection of shock finding algorithm or is a complicate process involving both the physical modules and the numerical algorithm in different work, much more carefully investigation is needed, which however, is out the scope of this work.

Combining with the result in the last subsection, our simulations suggest that the nu-

numerical viscosity smears out the shocks more seriously in regions outside of clusters than within clusters. As shocks are the sources of vorticity, numerical viscosity will significantly damp the vortices in regions outside of clusters, which may, to a great extent, be responsible for the differences regarding turbulence development in the IGM between two codes.

## 6. Discussions and Concluding Remarks

The evolution and properties of curl and compressive velocities, corresponding to the vorticity and divergence respectively, reveal the development history of turbulence in the IGM, and reflect the dynamical state of gas accreting onto different structures. The numerical viscosity embedded in numerical schemes may have significant impact on the vorticity and turbulent motions in the IGM in simulations. In this paper, we have addressed these two issues using a suite of simulations performed by two fixed mesh based codes that differ only in the spatial difference discretization, the second-order TVD scheme and the fifth-order positivity-preserving WENO scheme.

The development of turbulence in the IGM may undergo two phases. During the first supersonic phase, vortical motion is triggered by the baroclinity over strong curved external shocks. The scaling law in this phase follows Burgers’s  $k^{-2}$  law, which actually characterize turbulence consisting of strong shocks. In the second post-supersonic phase, vortices interact with each other and decay, although shocks are still formed. The governing dynamics for the vortices is subsonic. In the context of hierarchical structure formation history, the first phase may correspond to the stage that low density gas accretes onto sheets, filaments and clusters, while the second phase represents the interaction between gaseous protogalactic structures, e.g. merging processes. The growing history of the transit scale  $l_t$  and the upper end of the turbulence scale  $l_u$  as visualized in our simulation since  $z = 2$  may be a natural consequence of cosmic structure formation.

The turbulence development in the IGM may be affected by the numerical viscosity in two ways. Large scale velocity and density fluctuations in the baryonic matter would be damped, and hence the production of shocks and vortices in regions outside of clusters is suppressed. Namely, the turbulence injection rate is reduced by numerical viscosity. The kinetic turbulent energy transfer rate will also be reduced. On the other hand, the kinetic energy of large size vortices would be dissipated into thermal energy much more rapidly due to numerical viscosity, rather than cascading into small size eddies. In other words, the decaying rate is enhanced. The simulated dissipation scale,  $\sim 600h^{-1}\text{kpc}$ , in the TVD-512 run is significantly larger than  $\sim 300h^{-1}\text{kpc}$  in the WENO-512 run, indicating that the numerical dissipation might be comparable to the physical dissipation effects like shock heating and

Jeans dissipation under corresponding scale in the TVD-512 code. As a byproduct, the thermal and density evolution of gas accreting onto highly over-dense structures would also be changed by the numerical viscosity (e.g. Nelson et al. 2013).

The non-thermal pressure support, provided by the turbulent motions in the IGM, might slow down the accretion of baryon into dark matter structures during structure formation. Consequently, the baryon fraction in the highly turbulent regions would deviate from the cosmic mean. However, the situation would become more complicate in the presence of high level numerical viscosity. Both the compressible and vortical components of gas motions would be dissipated into thermal energy more rapidly. The lag in gas density fluctuation development with respect to dark matter may be caused by the non-thermal pressure support and the damping of compressible motions simultaneously.

The properties of turbulence in the IGM may be changed by many ingredients that are not considered in our simulations. The most important one may be the physical viscosity of the IGM. The baryonic gas is assumed to be non-viscous in our simulations, which also holds for almost all of the cosmological hydrodynamics simulations in the literature. The physical viscosity of the IGM is poorly known so far, although it is generally believed that the IGM should have very high Reynolds number(e.g. Gregori et al. 2012). However, the properties of turbulence in the IGM may change a lot from the simulation if the physical viscosity is non-negligible in the inertial range of this work, i.e.  $\sim 2h^{-1}\text{Mpc} - 200h^{-1}\text{kpc}$ . Simulation works shows that including the physical viscosity of the ICM would modify the pattern of gas flow and the evolution of gaseous sub-structures in the simulated clusters (Sijacki & Springel 2006; Dong & Stone et al. 2009; Suzuki et al. 2013). Tentative study suggests that the physical viscosity might be important on scales around tens of *kpc* (Brunetti & Lazarian 2007). Analysis of the morphology of filaments and bubbles in the Perseus cluster revealed by deep Chandra X-ray observation in Fabian et al.(2003a, 2003b) indicated that the hot ICM may have non-negligible viscosity and affects the cooling within the inner 50 *kpc* of the cluster. The expected dissipation scale due to physical viscosity is likely about tens of *kpc* and below the simulated dissipation scale  $\sim 200h^{-1}\text{kpc}$  in the WENO-1024 simulation. Future cosmological hydrodynamic simulations that implemented the physical viscosity properly would reveal more solid results on the development of turbulence in the IGM. In addition, including feedback from star formation, magnetic fields and AGN activity in the galaxies may trigger more intense turbulence below the dissipation scale. On the other hand, more precise constraints on the viscous properties and the turbulent motion in the IGM and ICM from observation are needed to verify the simulated results.

Finally, we summarize our results as follows,

- (1) The small-scale compressive ratio  $r_{CS}$  drops dramatically, from 0.84 at  $z = 2.0$  to

0.47 at  $z = 0.0$ , as the vorticity is effectively produced since  $z = 2$ , and can be comparable to the divergence at low redshifts. The curl velocity associated with the vorticity increases from  $\sim 10 \text{ km/s}$  at  $\rho_b \sim 1$  to  $\sim 90 \text{ km/s}$  at  $\rho_b \sim 100$  and is saturated henceforth for more dense region at  $z = 0.0$ , which is  $\sim 15 \text{ km/s}$  higher than the value that Oppenheimer & Dave (2009) used as the sub-resolution turbulence term to match the observation, and lower than observational upper limits by a factor of  $2 \sim 3$ . The estimated turbulence scale is 2Mpc down to 200kpc, which is consistent with ZFF2010.

(2) The power spectrum of the velocity field of the IGM shows two different phases within the turbulence scale range simultaneously, i.e., the supersonic phase and the post-supersonic phase. In the former regime, corresponding to  $\sim 0.2 - 0.68 h^{-1} \text{ Mpc}$  at  $z = 0$ , the scaling law follows  $k^{-1.88}$ ,  $k^{-2.20}$ ,  $k^{-2.02}$  for the total, compressive and curl velocity respectively, and is close to a Burgers turbulence. In the latter regime, i.e.,  $\sim 0.68 - 2.0 h^{-1} \text{ Mpc}$ , the power spectrum of the curl velocity transits to  $k^{-0.89}$ , while the other two are unchanged. The transition scale grows from  $\sim 0.32 h^{-1} \text{ Mpc}$  at  $z = 2.0$  to  $\sim 0.68 h^{-1} \text{ Mpc}$  at  $z = 0.0$ .

(3) The non-thermal pressure support, measured by the ratio of kinetic turbulent energy to internal energy, is comparable to the thermal pressure for  $\rho_b \simeq 10 - 100$ , or  $T < 10^{5.5} K$  at  $z = 0.0$ . The mean baryon fraction in different density bins of the IGM significantly deviates from the cosmic mean, and can be as low as 0.4 in regions that have the highest turbulent pressure support and the lowest compressive ratio.

(4) Relatively higher numerical viscosity would artificially dissipate both the compressive and vortical motions in the IGM more strongly. Consequently, the density fluctuation and vorticity are significantly damped in the TVD samples. The turbulence dissipation scale is remarkably shifted toward larger scale by a factor of 2, and hence shortens the turbulent inertial range. Numerical viscosity could lead to non-negligible uncertainty in the simulated thermal history of gas accretion during structure formation.

(5) The shocks in the regions outside clusters are significantly suppressed by relatively higher numerical viscosity since  $z = 2$  in the TVD samples. As cosmic shocks are the sources of vorticity, the different levels of turbulence in the IGM between two codes may be directly caused by the un-resolved shocks in the regions outside clusters in the TVD code.

Acknowledgements: The authors thank the anonymous referee for very useful comments. The simulations presented here were run on SGI Altix 4700 at Supercomputing Center of Chinese Academy of Sciences. WSZ thanks the support from China Postdoctoral Science Foundation and the Fundamental Research Funds for the Central Universities. This work is supported under the National Natural Science Foundation of China under grant 11203012, 11133001 and 10878010. Feng is supported by NSFC grant 11273060 and 91230115; Shu is

supported by ARO grant W911NF-11-1-0091 and NSF Grant DMS-1112700.

## A. Grid Difference Schemes

We first give a brief description of the positivity-preserving finite difference WENO scheme and then show its performance on two classical numerical tests, the shock-tube test and the Sedov blast wave test, comparing to the TVD scheme. We refer the interested reader to the references in this subsection for more details about the schemes.

### A.1. Positivity-Preserving WENO Scheme

In Zhang & Shu (2012), a simple limiting strategy is designed for high order finite difference WENO schemes, which can guarantee the positivity of density and pressure if they are positive initially, while also maintain the original high order accuracy of the scheme. The procedure is a generalization of an earlier strategy in Zhang & Shu (2010) for finite volume WENO schemes and discontinuous Galerkin methods. We will only give a brief description of this positivity-preserving procedure in this section, and refer the readers to Zhang & Shu (2012) for more details.

We first look at the one-dimensional Euler equation

$$w_t + f(w)_x = 0$$

with  $w = (\rho, \rho v, E)^T$  and  $f(w) = (\rho v, \rho v^2 + p, v(E + p))$ , where  $\rho$  is density,  $v$  is velocity,  $E$  is total energy, and  $p$  is pressure, which satisfies  $p = (\gamma - 1)(E - \frac{1}{2}\rho v^2)$  for a gamma-law gas. For a finite difference scheme, given the point values  $w_i^n$  at time level  $n$ , we let  $A_{i+\frac{1}{2}}$  denote the Roe average matrix of the two states  $w_i^n$  and  $w_{i+1}^n$ , and let  $L_{i+\frac{1}{2}}$  and  $R_{i+\frac{1}{2}}$  denote the left and right eigenvector matrices of  $A_{i+\frac{1}{2}}$  respectively, i.e.,  $A = R\Lambda L$  where  $\Lambda$  is the diagonal matrix with eigenvalues of  $A$  on its diagonal. Let  $\alpha = \max(|v| + c)$  where  $c$  is the sound speed, where the maximum is taken either globally for  $w_j^n$  over all  $j$  or locally for  $j$  over the the WENO reconstruction stencil. We use the Lax-Friedrichs flux splitting, namely

$$w^\pm = \frac{1}{2} \left( w \pm \frac{f(w)}{\alpha} \right). \quad (\text{A1})$$

At each fixed  $x_{i+\frac{1}{2}}$ , the algorithm proceeds as follows, where we omit the subscripts  $i + \frac{1}{2}$  for notational simplicity:

1. Let  $w^\pm(x) = \frac{1}{\Delta x} \int_{x-\Delta x/2}^{x+\Delta x/2} h^\pm(\xi) d\xi$ , then we are given the cell averages of  $h^\pm(x)$  by  $(\bar{h}^\pm)_j^n = (w^\pm)_j^n$ .

2. Transform all the cell averages  $(\bar{h}^\pm)_j^n$  for  $j$  in a neighborhood of  $i$  within the WENO reconstruction stencil to the local characteristic fields by setting  $(\bar{u}^\pm)_j^n = L(\bar{h}^\pm)_j^n$ .
3. Perform the WENO reconstruction for each component of  $(\bar{u}^\pm)_j^n$  to obtain approximations of the point values of the functions  $u^\pm = Lh^\pm$  at the point  $x_{i+\frac{1}{2}}$ . Notice that the stencil used for the WENO reconstruction for  $\bar{u}^+$  is  $\{i-2, i-1, i, i+1, i+2\}$ , and the one used for the WENO reconstruction for  $\bar{u}^-$  is  $\{i-1, i, i+1, i+2, i+3\}$ , due to upwind-bias for stability.
4. Transform back into physical space by  $h_{i+\frac{1}{2}}^\pm = Ru^\pm$ . A simple scaling limiter is then applied to  $h_{i-\frac{1}{2}}^+, h_{i+\frac{1}{2}}^-$  and an intermediate quantity to ensure positivity of density and pressure, see Zhang & Shu (2012) for the details. Then we form the numerical flux by  $\hat{f}_{i+\frac{1}{2}} = \alpha(h_{i+\frac{1}{2}}^+ + h_{i+\frac{1}{2}}^-)$ . The final scheme is

$$w_i^{n+1} = w_i^n - \lambda \left( \hat{f}_{i+\frac{1}{2}} - \hat{f}_{i-\frac{1}{2}} \right). \quad (\text{A2})$$

Combined with the third order TVD Runge-Kutta method, the scheme is guaranteed to maintain positivity of density and pressure. Generalization to multi-dimensions is straightforward in a dimension-by-dimension fashion.

## A.2. Test Examples

### (1) Shock tube test

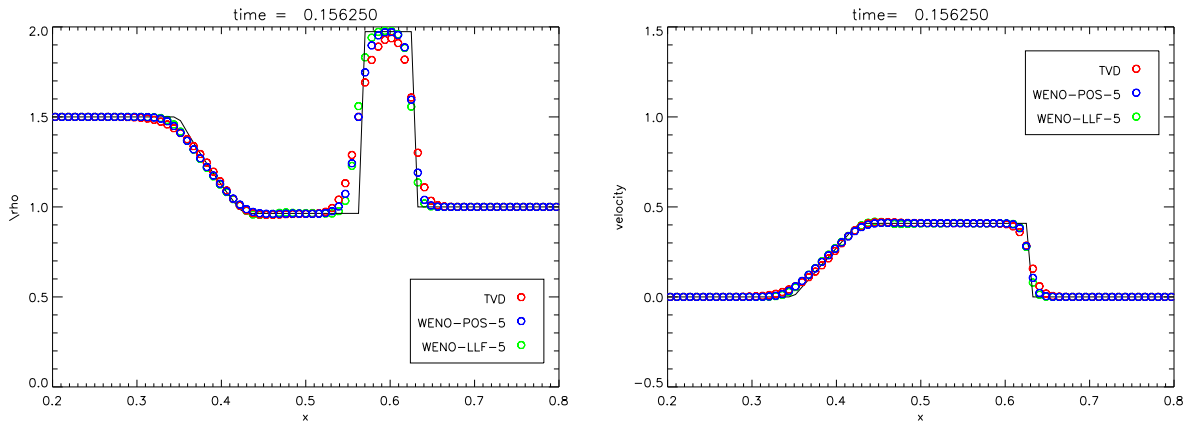


Fig. A1.— One dimensional shock tube test of the TVD and WENO schemes with resolution 128.

We present the results of the TVD and WENO schemes in solving the one-dimensional Sod shock tube problem with resolution 128 in Fig. A1. The initial state of the left and right region are given as  $(\rho_L = 1.5, v_1 = 0, p_L = 1.0)$  and  $(\rho_R = 1.0, v_2 = 0, p_R = 0.2)$  respectively. The polytropic index is 1.4. The CFL number is set to the same value 0.32. Both schemes can well capture the shock, although the TVD scheme shows more damping over the shock and the discontinuity surfaces. This result is not out of expectation, as the accuracy of the TVD scheme will degenerate over shocks more seriously than the WENO. The  $L^1$  errors for a smooth solution indicate that the TVD scheme achieve the order of 2.0 and the WENO-POS is 5.1. Also shown is the result run by the original fifth WENO scheme with the local Lax-Friedrichs flux splitting (WENO-LLF), which was used in ZFF2010 to study the turbulence in the IGM. The WENO-LLF code uses a CFL number 0.2 in order to keep it stable. Slightly improved performance is achieved by the WENO-LLF scheme at the cost of around 50% more cpu hours.

(2) Sedov blast wave test

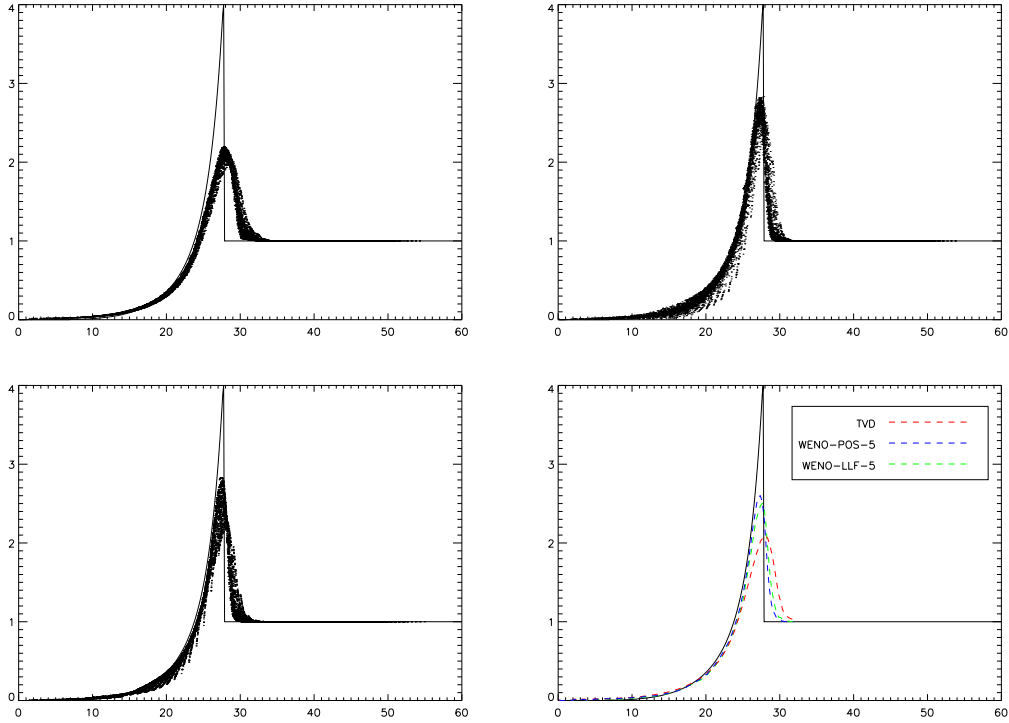


Fig. A2.— Density distribution of 20000 randomly selected grids in the three-dimensional Sedov blast-wave test with resolution  $256^3$ . Top left: TVD. Top right: WENO-POS-5. Bottom left: WENO-LLF-5. The bottom right panel shows the mean density as a function of radius in the three runs with respect to the analytical result (solid line).

Fig. A2. displays the density of randomly selected 20000 grid cells in three-dimensional Sedov blast-wave test with resolution  $256^3$ . The mean density as a function of radius is also shown in Fig. A2. The explosion front are captured by all the three schemes. However, it can be seen clearly that the fifth order WENO schemes resolve the explosion front more sharply, although moderate scattering appears at the central low density region. The density peaks in all the three codes are under-developed with respect to the analytic result, but the WENO schemes have smaller errors. The local flux splitting in WENO-LLF-5 shows more dispersion near the peak of the wave than the positive-preserving version.

### B. Resolution Convergence

We check the resolution convergence by comparing results in  $256^3$  and  $512^3$  samples. Only a few selected quantities are presented here for the sake of brevity. Fig. A3 shows the power spectra of vorticity and velocity. The pattern and difference between the WENO and TVD schemes are not changed by different resolution. The dissipation scale has been significantly extended by improved resolution.

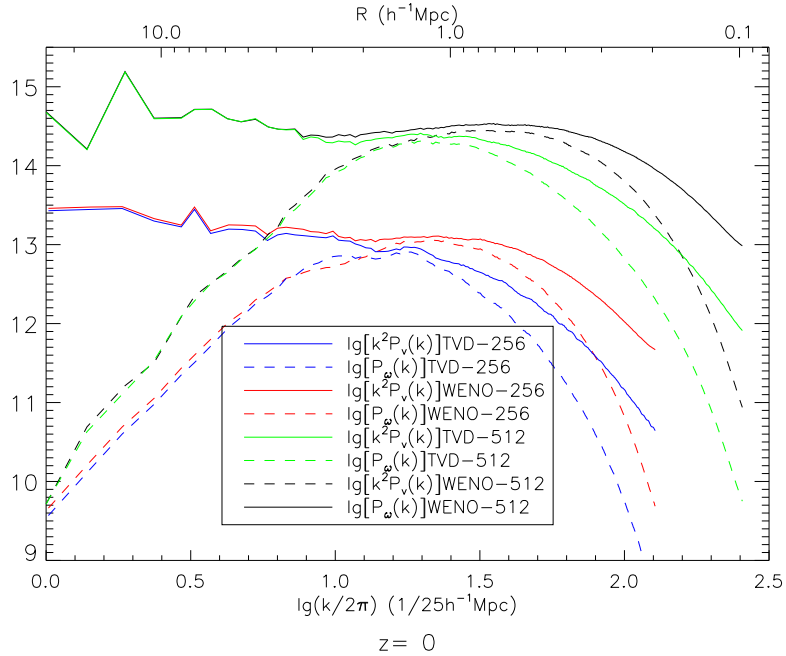


Fig. A3.— Power spectra of vorticity and velocity in  $256^3$  and  $512^3$  samples. The results of  $256^3$  samples have been shifted down by one dex for the sake of clarity.

Fig. A4 reports the kinetic turbulent energy ratio in the  $256^3$  run. The general trends are similar to results in  $512^3$ . The magnitude of the ratio is systematically lower than the



512<sup>3</sup> result, which results from a higher numerical viscosity for a lower resolution. Meanwhile, the kinetic turbulent energy ratio in the WENO-256 run is comparable to the TVD-512 run.

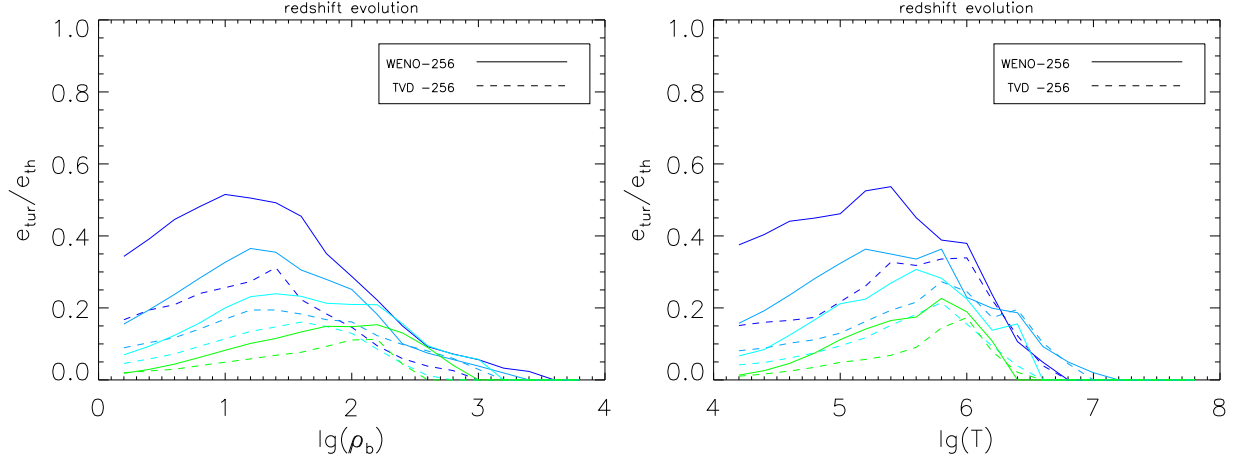


Fig. A4.— The ratio of kinetic turbulent energy to thermal energy as function of gas density (left) and temperature (right). Solid (dash) lines are the result in WENO-256 (TVD-256).

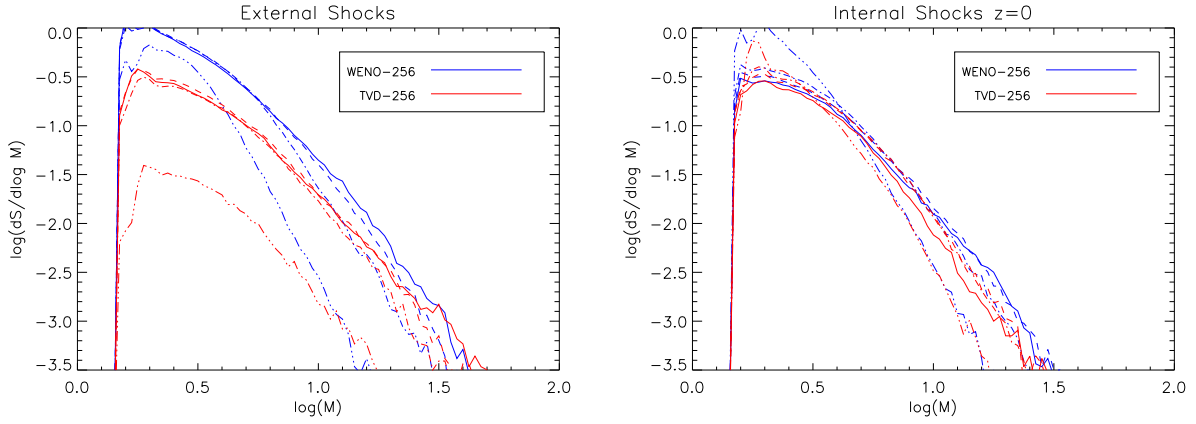


Fig. A5.— Surface area of external and internal shocks in the 256<sup>3</sup> simulations. Blue lines: WENO-256. Red lines: TVD-256. Solid (dash, dash-dotted, dash-triple-dotted) lines are the results at  $z = 0, 0.5, 1.0, 2.0$ .

Fig. A5 shows the distribution of external and internal shocks in the 256<sup>3</sup> samples. The difference is very similar to the 512<sup>3</sup> simulations, suggesting that the different levels of vorticity and turbulence between two codes at a given resolution may be mainly caused by the shocks outside of clusters.

## REFERENCES

- Agertz et al. 2007, MNRAS, 380, 963
- Batchelor, G.K. 1959, *The Theory of Homogeneous Turbulence*, (Cambridge University Press)
- Bauer, A., & Springel, V., 2012, MNRAS, 423, 2558
- Bregman, J.N., 2007, ARAA, 45, 221
- Brunetti, G., & Lazarian, A., 2007, MNRAS, 378, 245
- Bulbul, G. E., Smith, Randall K., Foster, A., et al., 2012, ApJ, 747, 32
- Cen, R.Y., & Ostriker, J.P., 1999, ApJ, 514, 1
- Cen R.Y., & Ostriker J.P., 2006. ApJ, 650,560
- Churazov E., Forman W., Jones C., Sunyaev R., Bohringer H., 2004, MNRAS, 347, 29
- Dave, R., Hernquist, L., Katz, N., & Weinberg, D.H., 1999, ApJ, 511, 521
- Dave R, Cen R.Y., Ostriker J.P., Bryan G.L., Hernquist L., et al., 2001, ApJ, 552, 473
- Dolag, K., Vazza, F., Brunetti G., & Tormen G. 2005, MNRAS, 364, 753
- Dong, R.B., Stone, J. M., 2009, ApJ, 704, 1309
- Evoli, C., & Ferrara, A., 2011, MNRAS, 413, 2721
- Fabian, A. C., Sanders, J. S., Allen, S. W., Crawford, C. S., et al., 2003a, MNRAS, 344, L43
- Fabian, A. C., Sanders, J. S., Crawford, C. S., Conselice, C. J., et al., 2003b, MNRAS, 344, L48
- Federrath, C., Roman-Duval, J., Klessen, R. S., Schmidt, W., Mac Low, M.-M., 2010, A&A, 512, A81
- Feng, L.L., Shu, C.-W., & Zhang, M.P. 2004, ApJ, 612, 1
- Fukugita, M., Hogan, C.J., & Peebles, P.J.E. 1998, ApJ, 503, 518
- Gregori et al. , 2012, Nature, 481, 480
- Harten, A., 1983, J. Comp. Phys., 49, 357
- He, P., Liu, J., Feng, L.L., Shu, C.-W., & Fang, L.Z. 2006, Phys. Rev. Lett, 96, 051302
- Iapichino, L., Schmidt, W., Niemeyer, J.C., & Merklein, J., 2011, MNRAS, 414, 2297
- Jiang, G. & Shu, C.-W, 1996, J. Comp. Phys, 126, 202
- Jones, Bernard. J. T., 1999, MNRAS, 307, 376
- Kida, S. & Orszag, S.A. 1990, J. Sci. Comput., 5, 85

- . 1992, *J. Sci. Comput.*, 7, 1
- Komatsu, E., et al. 2009, *ApJS*, 180, 330
- Kritsuk, A.G., Norman, M.L., Padoan, P., & Wagner, R., 2007, *ApJ*, 665, 416
- Landau, L., & Lifshitz, E. 1959, *Fluid Mechanics*, (Pergamon Press)
- Matarrese, S., & Mohayaee, R., 2002, *MNRAS*, 329, 37
- Miniati, F., Ryu, D., Kang, H., Jones, T.W., et al, 2000, *ApJ*, 542, 608
- Nelson, D., et al. 2013, arXiv:1301.6753
- Oppenheimer B.D., Dave R., 2009, *MNRAS*, 395, 1875
- Pfrommer C., Springel V., Enlin T.A., & Jubelgas M., 2006, *MNRAS*, 367, 113
- Porter, D.H., Pouquet, A., & Woodward, P.R. 1992a, *Theor. Comput. Fluid Dyn.*, 4, 13
- . 1994, *Phys. Fluids*, 6, 2133
- Porter, D.H., Woodward, P.R., & Pouquet, A. 1998, *Phys. Fluids*, 10, 237
- Ryu, D., Kang, H., Cho, J., & Das, S. 2008, *Science*, 320, 909
- Ryu D., Kang H., Hallman E., & Jones T.W., 2003, *ApJ*, 593, 599
- Ryu, D., Ostriker, J.P., Kang, H., & Cen, R.Y. 1993, *ApJ*, 414, 1
- Sagaut, P., & Cambon, C, 2008, *Homogeneous Turbulence dynamics*, (Cambridge University Press)
- Sanders, J. S., Fabian, A. C., 2013, *MNRAS*, 429, 2727
- Sanders, J. S., Fabian, A. C., Smith, R. K., 2011, *MNRAS*, 410, 1797
- Sanders, J. S., Fabian, A. C., Smith, R. K., & Peterson, J. R., 2010, *MNRAS*, 402, 11
- Schmidt, W. 2007, arXiv:0712.0954v1
- Schmidt, W. et al. 2009, *A&A*, 494, 127
- Shen J., Abel T., Mo H.J., & Sheth R.K., 2006, *ApJ*, 645, 783
- Shu, C.-W. 1998, in *Lecture Notes in Mathematics*, volume 1697, 325, (Springer).
- Shu, C.-W. 1999, in *Lecture Notes in Computational Science and Engineering*, volume 9, 439 (Springer).
- Sijacki, D., & Springel, V., 2006, *MNRAS*, 371, 1025
- Skillman, S. W., O’Shea, B. W. Hallman, E. J., Burns, J. O., & Norman, M. L., 2008, *ApJ*, 689, 1063
- Strang, G. 1968, *SIAM J. Numer. Anal.*, 5, 506

- Suzuki, K., Ogawa, T., Matsumoto, Y., & Matsumoto, R., 2013, *ApJ*, 768, 175
- Tepper-Garcia, T., Richter, P., Schaye, J., Booth, C.M. et al., 2011, *MNRAS*, 413, 190
- Theuns, T., Leonard, A., Efstathiou, G., Pearce, F. R., & Thomas, P. A. 1998, *MNRAS*, 301,478
- Vazza, F., Brunetti, G., & Gheller, C., 2009, *MNRAS*, 395, 1333
- Vazza, F., Dolag, K., Ryu, D., Brunetti, G. et al., 2011, *MNRAS*, 418, 960
- Zhang, X., & C.-W. Shu, 2010, *J. Comp. Phys*, 229, 8918
- Zhang, X., & C.-W. Shu, 2012, *J. Comp. Phys*, 231, 2245
- Zheng, W., et al. 2004, *ApJ*, 605, 631
- Zhu, W.S., Feng, L.L., & Fang, L.Z., *ApJ*, 2010, 712, 1 (ZFF2010)
- Zhu, W.S., Feng, L.L., & Fang, L.Z., *MNRAS*, 2011, 415, 1093